ELSEVIER

Journal of Volcanology and Geothermal Research 67 (1995) 233–262

Journal of volcanology and geothermal research

Mid-Atlantic Ridge volcanism from deep-towed side-scan sonar images, 25°–29°N

Deborah K. Smith [a,*], Joe R. Cann [b], Martin E. Dougherty [c], Jian Lin [a], Sara Spencer [d], Chris MacLeod [e], Jane Keeton [f], Eddie McAllister [b], Benjamin Brooks [g], Rachel Pascoe [b], Wanda Robertson [h]

[a] *Department of Geology and Geophysics, Woods Hole Oceanographic Institution, Woods Hole, MA 02543USA*
[b] *Department of Earth Sciences, University of Leeds, Leeds LS2 9JT UK*
[c] *Department of Geosciences, Boise State University, Boise, ID 83725 USA*
[d] *American University, Beirut Lebanon*
[e] *Institute of Oceanographic Sciences Deacon Laboratory, Wormley, Surrey GU8 5UB UK*
[f] *Department of Geological Sciences, Durham University, Durham City, DH1 3LE UK*
[g] *Department of Geological Sciences, Cornell University, Ithaca, NY 14853 USA*
[h] *University of North Alabama, Florence, AL 35633 USA*

Received 6 May 1994; accepted 17 August 1994

Abstract

We present deep-towed side-scan sonar mosaics of the inner valley floor of eight spreading segments at the slow-spreading Mid-Atlantic Ridge between 25° and 29°N. An analysis of these images, which well-resolve features a few tens of meters in size, confirms that the multitude of small seamounts, with diameters between 0.5 and 3 km identified on the inner valley floor from previously collected multibeam bathymetry data, are volcanically constructed. Moreover, these images reveal that these volcanoes have distinct surface morphologies not evident in the coarser resolution multibeam bathymetry maps: 83% of the seamounts have a hummocky (bulbous) morphology; the other 17% have a smooth morphology. In addition to near-circular seamounts, small (1–2 km long) volcanic ridges are abundant in our study regions, and are not, in general, seen in the bathymetry maps. We combine these new morphological data with existing models for the construction of the shallow oceanic crust to obtain a better understanding of the melt delivery system that builds the distinctive seafloor topography at the slow-spreading Mid-Atlantic Ridge.

1. Introduction

The study of seafloor volcanic features produced at mid-ocean ridges provides information on crustal melt supply and delivery to the ridge. To understand these processes better at the slow-spreading Mid-Atlantic Ridge (MAR), we collected high-resolution side-scan sonar images of the axial zone between 25° and 29°N. In this paper we focus on the multitude of small volcanic edifices observed on the inner valley floor. These individual volcanoes with length scales between 0.5 and 3 km have varied and distinct volcanic morphologies and shapes (e.g., Kong et al., 1988; Smith and Cann, 1992), and they commonly overlap and pile up to build larger axial volcanic ridges (e.g., Ballard and van Andel, 1977; Karson et al., 1987; Smith and Cann,

* Corresponding author.

SSDI 0377-0273(94)00086-7

1990, 1992). Understanding their formation is essential to understanding how the oceanic crust is constructed at this slow-spreading ridge.

Mapping of the axis of the MAR using multibeam echo-sounders has now been accomplished in a number of regions (e.g., Ballard and van Andel, 1977; Karson et al., 1987; Purdy et al., 1990; Grindlay et al., 1991; Detrick et al., 1995). Multibeam bathymetry data provide an excellent overview of the topography, and have been used to investigate the distributions and abundances of near-axis volcanoes in both the South and North Atlantic (e.g., Batiza et al., 1989; Epp and Smoot, 1989; Smith and Cann, 1990, 1992). The spatial resolution of the multibeam data is coarse (~ 150 m footprint), however, and using them to discriminate between volcanically and tectonically produced edifices is, in some places, difficult.

To refine the volcanological inferences made from our earlier investigation of near-circular volcanoes (seamounts) at the MAR between the Kane and Atlantis transforms (Smith and Cann, 1990, 1992), we obtained deep-towed side-scan sonar data in four study areas within the existing bathymetry coverage (Fig. 1). These data well-resolve features a few tens of meters in diameter. Deep-towed side-scan sonar data have been collected at the MAR prior to this (e.g., Macdonald and Luyendyk, 1977; Kong et al., 1988; Searle et al., 1992; Parson et al., 1993); our data are unique, however, in that they provide complete coverage of the inner valley floor of the median valley along major portions of eight spreading segments. Such extensive high-resolution coverage has not been obtained previously, primarily due to the effort of mapping the wide (10–15 km) axial zone.

An analysis of the side-scan sonar images confirms that seamounts identified from the bathymetry data are volcanically constructed. In addition, they reveal that seamounts have distinct surface morphologies not evident in the coarser resolution multibeam data: 83% of the seamounts identified in the side-scan sonar data have a hummocky (bulbous) morphology; the remainder have a smooth morphology. (Whether these morphologies are constructed from pillow or sheet flows can not be determined from the side-scan sonar data, however.) The sonar images also reveal that small (1–2 km long) volcanic ridges occur throughout the study areas. In most cases, these features can not be identified in the bathymetry maps.

In this paper we present the side-scan sonar mosaics of each study area and discuss their general characteristics. We then present detailed images of the two morphological types of seamounts (hummocky and smooth), examine the characteristics of their populations, and discuss the possible controls on their formation. Next, we describe and classify the numerous small volcanic ridges that cover the inner valley floor of our study areas. Finally, we incorporate this new morphologic information provided by the side-scan sonar images into existing models for building the crust at the slow-spreading MAR.

2. Overview of Mid-Atlantic Ridge topography and summary of previous work

The slow (~ 25 mm/yr full rate)-spreading MAR between 20°and 40°N is composed of discrete spreading segments tens of kilometers long (e.g., Ramberg and van Andel, 1977, Ramberg et al., 1977; Purdy et al., 1990; Sempere et al., 1990, 1993) (Fig. 1). The large-scale topography of the ridge is dominated by a major rift valley. The inner floor of the rift, whose edges can be defined structurally as the first major fault scarp, is the primary site of crustal construction (e.g., Macdonald, 1977). Understanding the volcanic processes and, in particular, the volcanic products formed on the inner valley floor is the main focus of this study.

Most, but not all, segments contain prominent axial volcanic ridges within their inner valley floors that are the principal sites of lava extrusion. Between the Kane and Atlantis transforms only Segment 6 (Fig. 1) has no axial volcanic ridge. South of the Kane transform, the "southern cell" of Kong et al. (1988) also lacks an axial ridge. Axial volcanic ridges show a wide spectrum of styles; they can be discontinuous along the strike of the segment, and can range in size up to several hundreds of meters high, several kilometers wide and tens of kilometers long (Ballard and van Andel, 1977; Ramberg and van Andel, 1977; Karson et al., 1987; Sempere et al., 1990, 1993; Smith and Cann, 1990, 1992, 1993). The widespread occurrence of axial volcanic ridges on the inner valley floor indicates that their construction is the preferred style of large-scale volcanism in the axial zone.

Near-circular volcanic edifices (seamounts) with diameters between 0.5 and 3 km, are distributed over

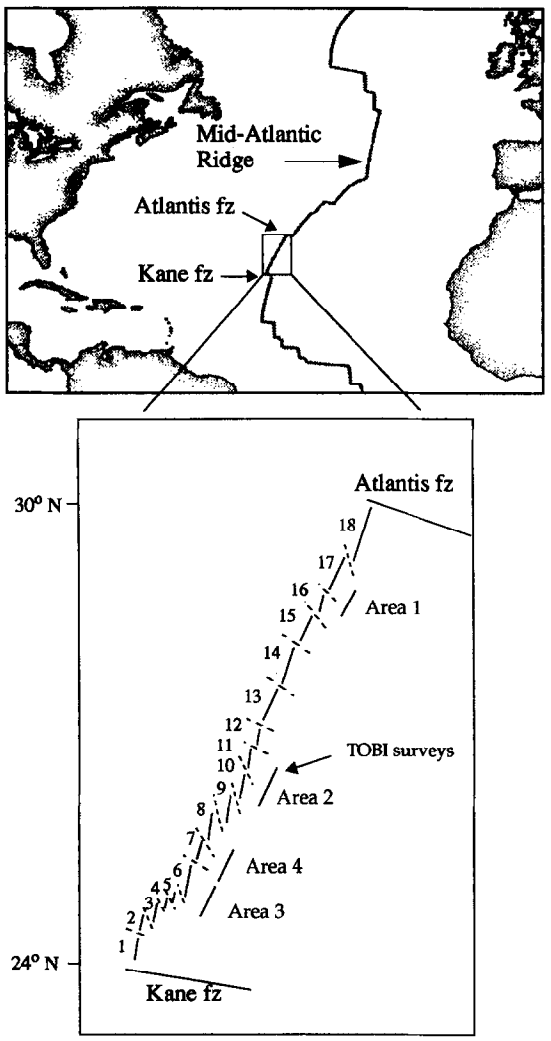

Fig. 1. Location map showing the northern Mid-Atlantic Ridge. The box indicates the area between the Kane and Atlantis transforms that has been the site of detailed multibeam bathymetry surveys (Purdy et al., 1990). The lower panel is an enlargement of the region within the box. Straight lines show the location of the ridge axis; dashed lines show ridge segment boundaries. Numbers correspond to individual spreading segments that have been defined from the bathymetry. Lines to the right of the axis indicate the along-axis extent of the four study areas that have been surveyed using the TOBI deep-towed side-scan sonar instrument.

the valley floor of all spreading segments. Most of them are associated with the large-scale axial volcanic ridges (Crane and Ballard, 1981; Karson et al., 1987; Kong et al., 1988; Brown and Karson, 1988; Smith and Cann, 1990, 1992; Sempere et al., 1993). In some segments chains of seamounts mark the tops of the axial volcanic ridges. In other segments they occur along the top and sides of the volcanic ridge. In segments without axial volcanic ridges, seamounts are scattered across the valley floor (Kong et al., 1988; Smith and Cann, 1992).

As a step towards understanding the formation of these small volcanoes and their relationship to the larger axial volcanic ridges, Smith and Cann (1990, 1992) characterized the abundances, distributions and shapes of nearly 500 seamounts with heights in the range 50–350 m identified in multibeam bathymetry data from the inner valley floor between the Kane and Atlantis transforms (Fig. 1). They suggested that each of the seamounts was fed from a point source and that, in combination with flows, seamounts pile up and coalesce to construct the large axial volcanic ridges. Furthermore, based on their interpretation of the multibeam data and combined with existing seismic and geochemical studies (e.g., Whitmarsh, 1973; Bryan and Moore, 1977; Nisbet and Fowler, 1978; Fowler and Keen, 1979; Purdy and Detrick, 1986; Toomey et al., 1988; Huang and Solomon, 1988; Kong et al., 1992), Smith and Cann suggested that beneath the MAR magma rises buoyantly within the crust to the sharp rheological transition at the base of the brittle lid, where it is trapped to form small bodies, each of which then feeds one or a few seamounts. They argued that, if the MAR is fed by small ephemeral magma pockets, the structure of the lower crust will be substantially different than if it were fed by a single long-lived magma chamber (as speculated for the faster-spreading East Pacific Rise). The crust will be composed of a multitude of small plutonic bodies, each linked to a surface volcanic feature by a feeder dike or pipe, and each having cooled separately.

The collection of the deep-towed side-scan sonar surveys presented in this paper led directly from the work of Smith and Cann (1990, 1992). Our intention was to refine our interpretation of the bathymetry data by obtaining high-resolution images of the volcanic morphology within the multibeam coverage and over the entire width of the inner valley floor.

3. Data description and study areas

The deep-towed side-scan sonar data presented in this paper were collected in 1992 aboard the RRS *Charles Darwin* using the Towed Ocean Bottom Instru-

Table 1
Characteristics of the four study areas

Study area	Segment number	Segment length (km)	Segment width[a] (km)	Along-axis shallowing[b] (m)	Along-axis MBA variation[c] (mGal)	Seamount density[d] (per 10^3 km^2)
1	17	60	6.5	750	−20	110
	16	15	15	–	−7	76
2	11	40	7.5	600	−15	133
	10	45	6	750	−10	67
3	6	55	7.5	750	−22	84
4	8	42	12	500	−16	48
	7	35	10	500	−9	88

[a]Width averaged along the axis.
[b]Measured from segment end to shallowest depth running along the center of the inner valley floor.
[c]MBA = mantle Bouguer anomaly, variation calculated from the end of the segment to the center of the low. Area 1 values from Lin et al. (1990).
[d]From Smith and Cann (1992).

ment (TOBI) which was developed and is operated by the Institute of Oceanographic Sciences Deacon Laboratory. TOBI deep-towed side-scan sonar operates at a frequency of 30/32 kHz, and collects a swath of data 6 km wide. The TOBI vehicle is towed 400–600 m from the seafloor. The resolution of the side-scan images is a function of range, but in general the image pixel size is about 10 m so that features with diameters a few tens of meters or greater are well resolved. In addition to the side-scan sonar, the TOBI vehicle housed a 7.5-kHz sub-bottom profiler and a triaxial magnetometer. Shipboard gravity data were also collected during the surveys. In conjunction with the collection of geophysical data, a dredging program was also accomplished; these data will be presented in another paper.

Four study areas were selected within the existing multibeam bathymetry coverage (Fig. 1). The characteristics of each study region are described below and summarized in Table 1. The areas were selected after a detailed examination of all 18 segments between the Kane and Atlantis transforms and provide a cross-section of the different characteristics observed. The segments in our study areas, therefore, exhibit a wide range in overall topographic parameters (e.g., size of the axial volcanic ridge, width and length of the inner valley floor, characteristics of the seamount population). Sea-

Fig. 2. Area 1 bathymetry (a), side-scan sonar data (b), and geologic interpretation (c). (a) Top panel shows the bathymetry for Study Area 1. Individual swaths collected along ship tracks can be seen. Shadings represent water depth as shown to right. Contours are plotted every 200 m. The white lines show the tracks of the TOBI vehicle. The lower panel also shows the TOBI tracklines. The spreading segments are marked and the boundary between them is shown by a dashed line. The solid dark contour represents the bounding scarp of the inner valley floor; it is defined here as the first major fault (>200 m in relief). Triangles plotted within the valley floor are the locations of seamounts identified in the multibeam bathymetry by Smith and Cann (1992); shading corresponds to seamount surface morphology. Black triangles show the locations of hummocky seamounts; open triangles show the locations of smooth seamounts; and shaded triangles show those seamounts that could not be identified in the side-scan sonar data. (b) Side-scan sonar mosaic of Area 1 composed of three overlapping swaths. The mosaics were constructed by hand, and photographed. The track of the TOBI vehicle is at the center of a swath; scalloping along the track is an artifact caused by a bottom tracking problem. In general, data located within 500 m either side of the vehicle track are considered unreliable. Bright is a reflection, and dark is a shadow or attenuated return from sediment covered terrain. Where two swaths overlap, the swath shown was selected (in most cases) so that the illumination direction is from the center of the mosaic. The spreading segments are labelled with numbers corresponding to those shown on Fig. 1. The boundary between segments is shown with a dashed line. Only features that are distinctive at this scale are marked. Bright linear reflectors are inferred to be faults; bright regions near the ends of segments are interpreted to be landslide zones. Two seamounts are marked in Segment 17. The southern one is ~350 m in relief. It is the tallest seamount identified by Smith and Cann (1992) between the Kane and Atlantis transforms. The seamount to the north is ~220 m in relief and has a large summit crater. Detailed images of these two seamounts are given in Fig. 9a. (c) Geologic interpretation of the side-scan sonar mosaic in (b). The same features are marked on both. In addition, the approximate location of the axial volcanic ridge is shaded.

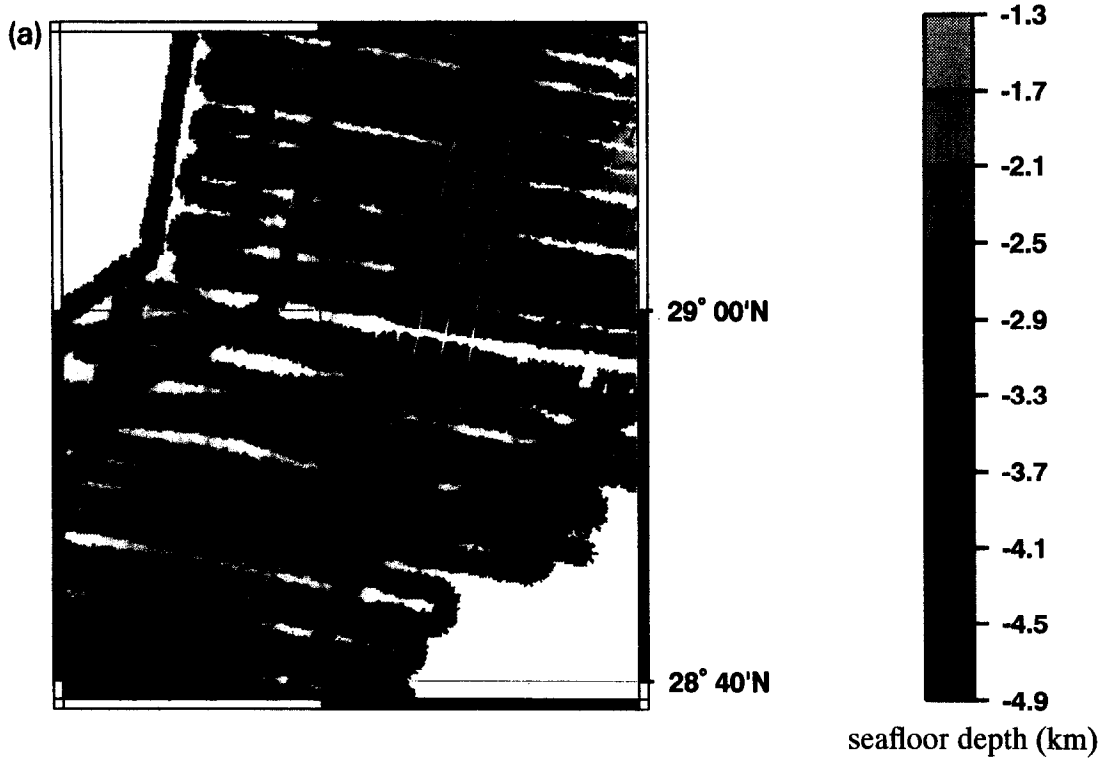
(a)
29° 00'N
28° 40'N
-1.3
-1.7
-2.1
-2.5
-2.9
-3.3
-3.7
-4.1
-4.5
-4.9
seafloor depth (km)

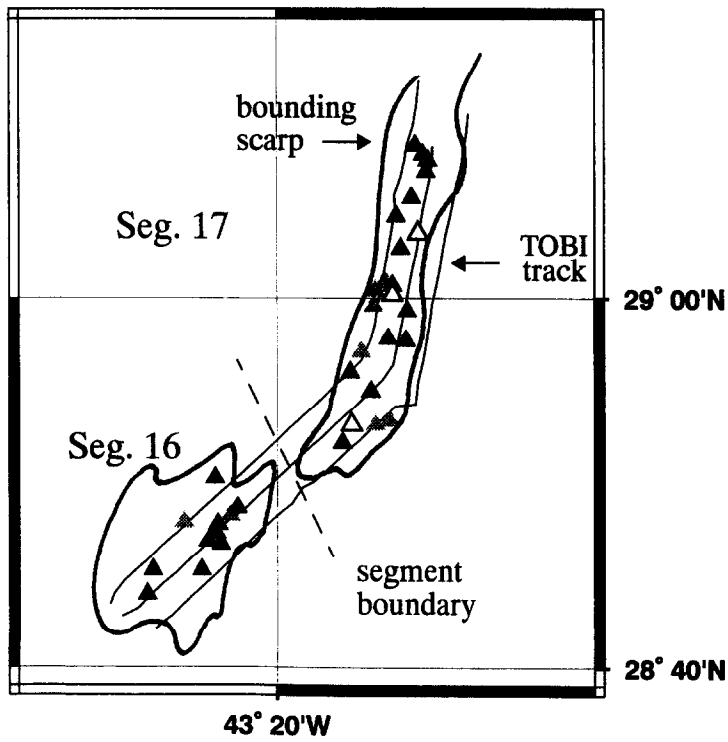
bounding
scarp
Seg. 17
TOBI
track
29° 00'N
Seg. 16
segment
boundary
28° 40'N
43° 20'W

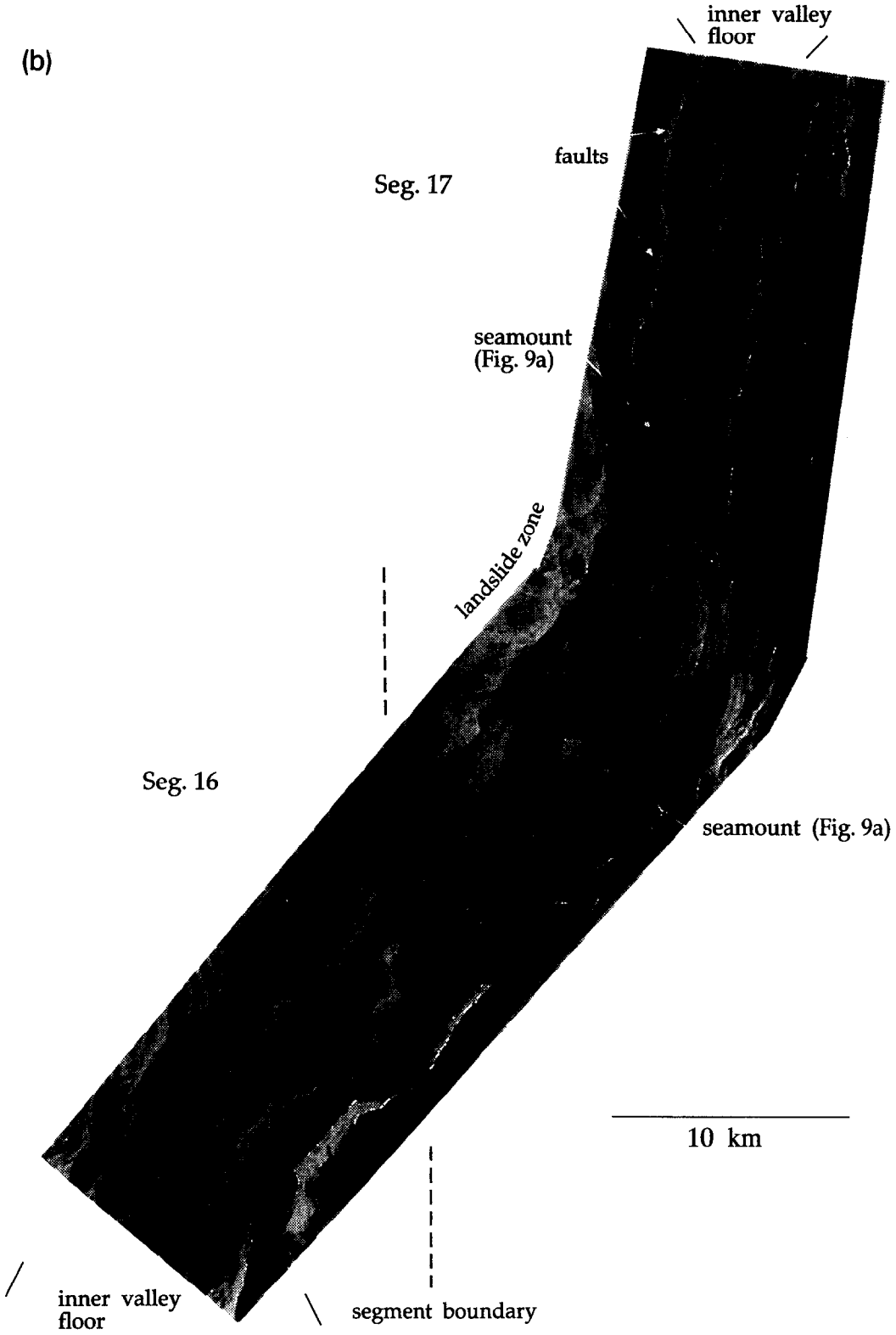

Fig. 2 (continued).

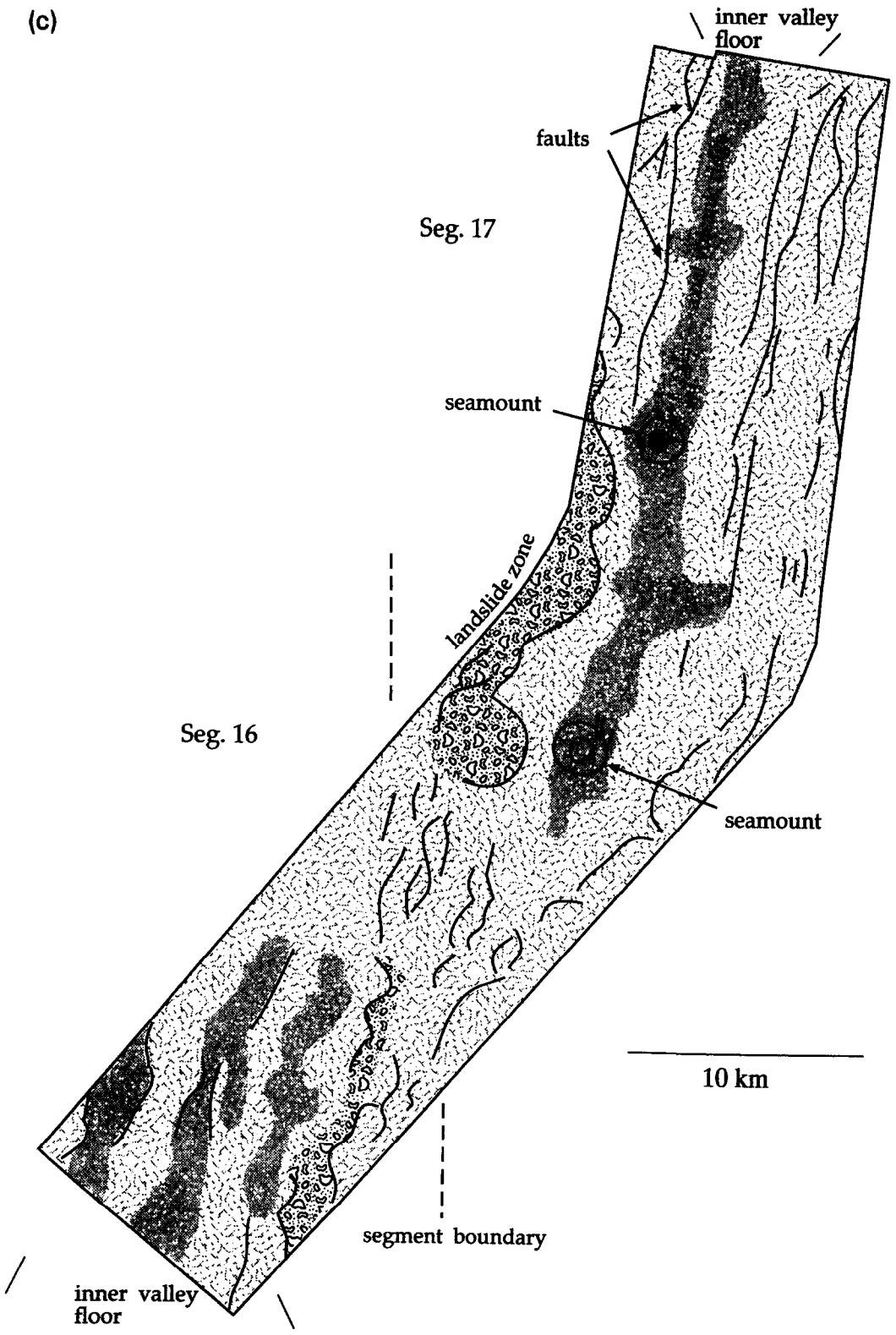

Fig. 2 (continued).

Table 2
TOBI side-scan sonar coverage

Study area	Area surveyed (km^2)
1	690
2	700
3[a]	1130
4	1120
Total	3640

[a]Segment 6 only.

mount densities are also given in Table 1. These values are from Smith and Cann (1992) and represent the number of seamounts identified on the inner valley floor of each segment normalized to area surveyed. In addition, Table 1 lists the along-axis variation in mantle Bouguer gravity anomaly for each segment. A large negative anomaly is generally associated with thicker crust or higher mantle temperatures or both (e.g., Kuo and Forsyth, 1988; Lin et al., 1990).

The multibeam bathymetry data and side-scan sonar mosaics for each area are presented in Figs. 2–5. The track lines of the TOBI surveys are displayed on the bathymetry maps of each area. Within each of the areas the surveys were designed to image the entire width of the inner valley floor and parts of the first fault block of the median valley walls. To accomplish this the ship tracks were selected to get better than 100% coverage. During the surveys, the ship was navigated using the multibeam bathymetry data. In total, over 3600 km^2 of side-scan sonar images of the inner valley floor and first step of the bounding walls were obtained (Table 2).

The side-scan sonar mosaics presented in Figs. 2–5 were constructed by hand from individual swaths and photographed. Each swath is 6 km wide; bright is a reflection, dark is a shadow or attenuated return. The inner valley floor can be seen in these mosaics as a region of relatively bright backscatter returns. The volcanic morphology of the inner valley floor appears, in all but Segment 6, to be dominated by a hummocky or bulbous texture. Single hummocks range in size with diameters $50 \leq d \leq 500$ m. These features are not well defined in the multibeam data. Individual volcanic edifices that are distinctive at this scale are labelled on the mosaics. Outside the inner valley floor linear, narrow reflectors are inferred to be fault scarps of the median valley walls. Large regions of high reflectivity are landslide zones. The low backscatter seen in the valley walls is most likely caused by sediment buildup which attenuates the signal. Each mosaic has an accompanying sketch marking the location of the segments and boundaries between them, the axial volcanic ridge, some of the major faults, landslide zones, and a few specific volcanic edifices.

3.1. Area 1

Area 1 is composed of the southern half of Segment 17 and most of Segment 16 (Fig. 2). Segments 16 and 17 are offset by approximately 7 km, and separated by a faulted ridge (septum) (Spencer et al., 1992).

Segment 17 is approximately 60 km long; the inner valley floor is, on average, 6.5 km wide. Segment 17 shallows along the axis approximately 750 m from the ends to center. A large negative, mantle Bouguer anomaly (approximately 20 mGal variation along the segment) is located near the center of the segment (Lin et al., 1990). An axial volcanic ridge runs most of the length of the inner valley floor; in places it is asymmetrically located to the west between the bounding scarps. The volcanic ridge widens and narrows along its length, but is typically a few kilometers wide and about 150 m high; seamounts are scattered along it. The tallest seamount identified by Smith and Cann (1992) between the Kane and Atlantis transforms ($\sim$350 m in relief) is located near the southern terminus of the axial volcanic ridge and is marked on Fig. 2. Another seamount north of this one is about 220 m in relief and has a large crater at the top. These two volcanoes sit within the axial volcanic ridge, but rise well above its average height of 150 m. Other seamounts are not as easily distinguished in the mosaics at this scale. Seg-

Fig. 3. Area 2 bathymetry (a), side-scan sonar data (b), and geologic interpretation (c). (a) Bathymetry and locations of identified seamounts are shown. See Fig. 2 for description of the data and shade coding of triangles. (b) Side-scan sonar mosaic of Area 2 composed of three overlapping swaths. See Fig. 2 for description of the data. Because of the dominance of hummocky topography in Area 2, individual volcanic edifices are hard to see at this scale. One seamount, located in a gap in the axial volcanic ridge is marked. It is approximately 70 m high, and has a summit crater at the top. A detailed image of this feature is shown in Fig. 9b. (c) Geologic interpretation of the side-scan sonar mosaic in (b). The same features are marked on both. In addition, the approximate location of the axial volcanic ridge is shaded.

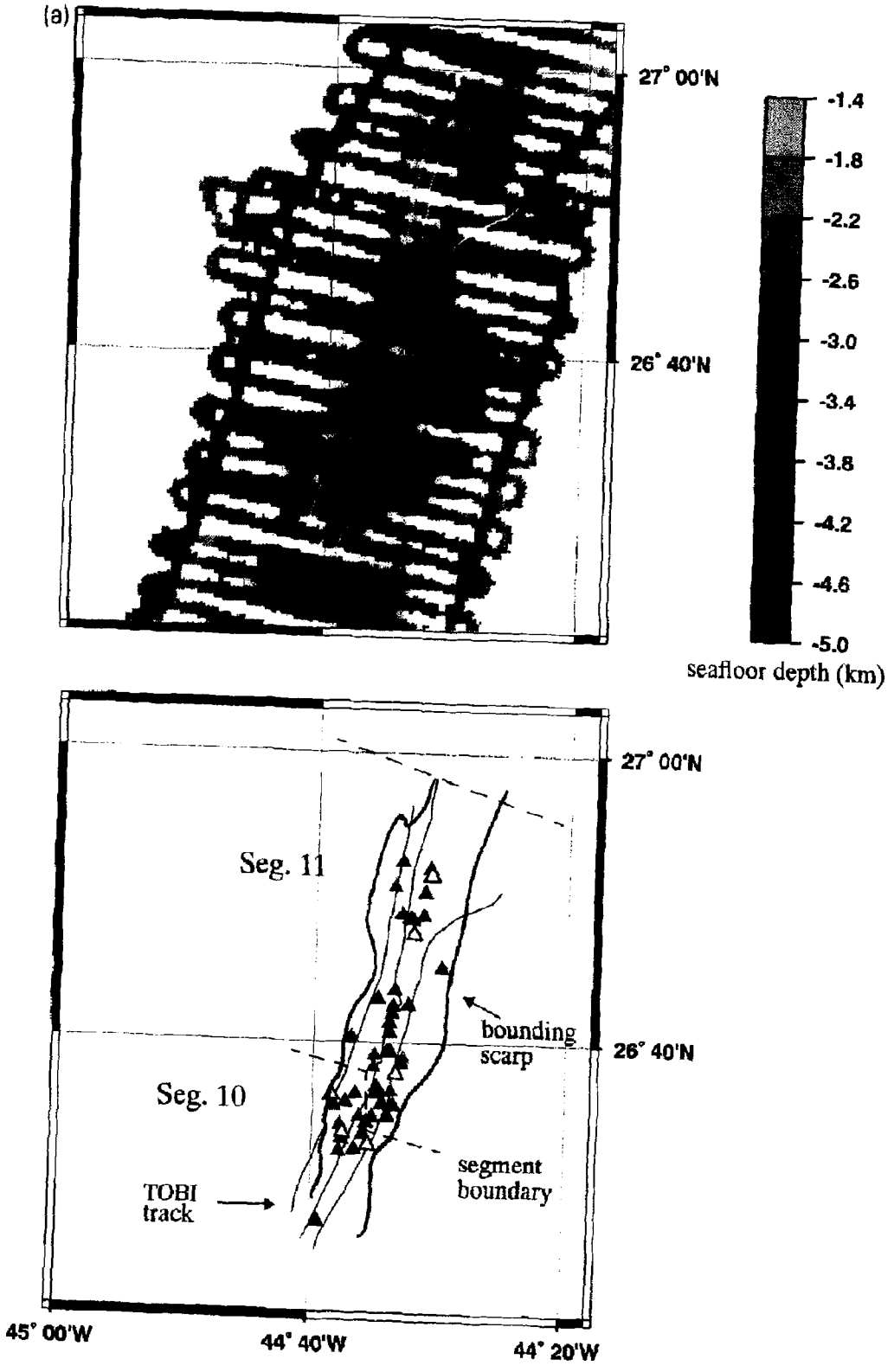
(a)
27° 00'N
26° 40'N
-1.4
-1.8
-2.2
-2.6
-3.0
-3.4
-3.8
-4.2
-4.6
-5.0
seafloor depth (km)
27° 00'N
Seg. 11
bounding scarp
26° 40'N
Seg. 10
segment boundary
TOBI track
45° 00'W
44° 40'W
44° 20'W

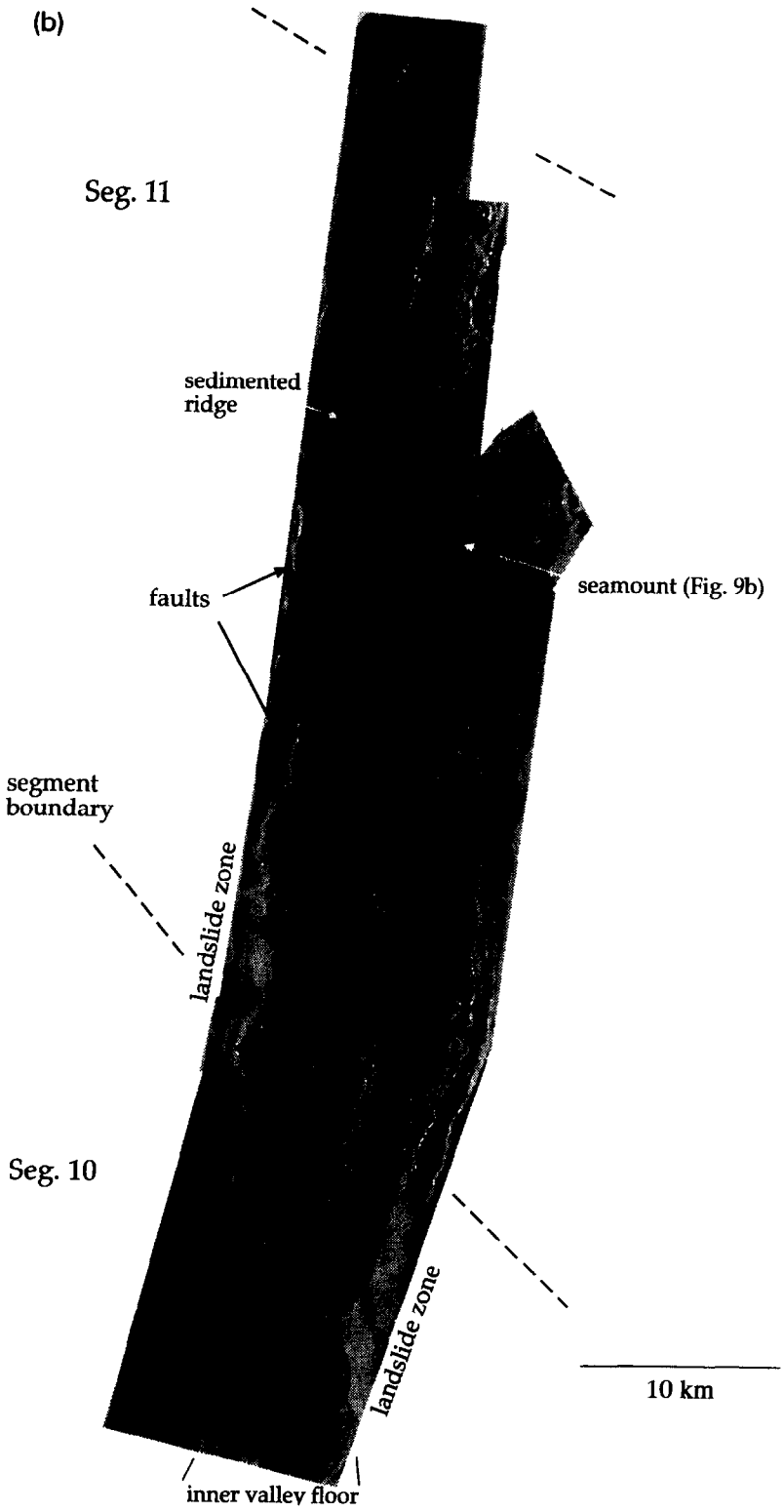

Fig. 3 (continued).

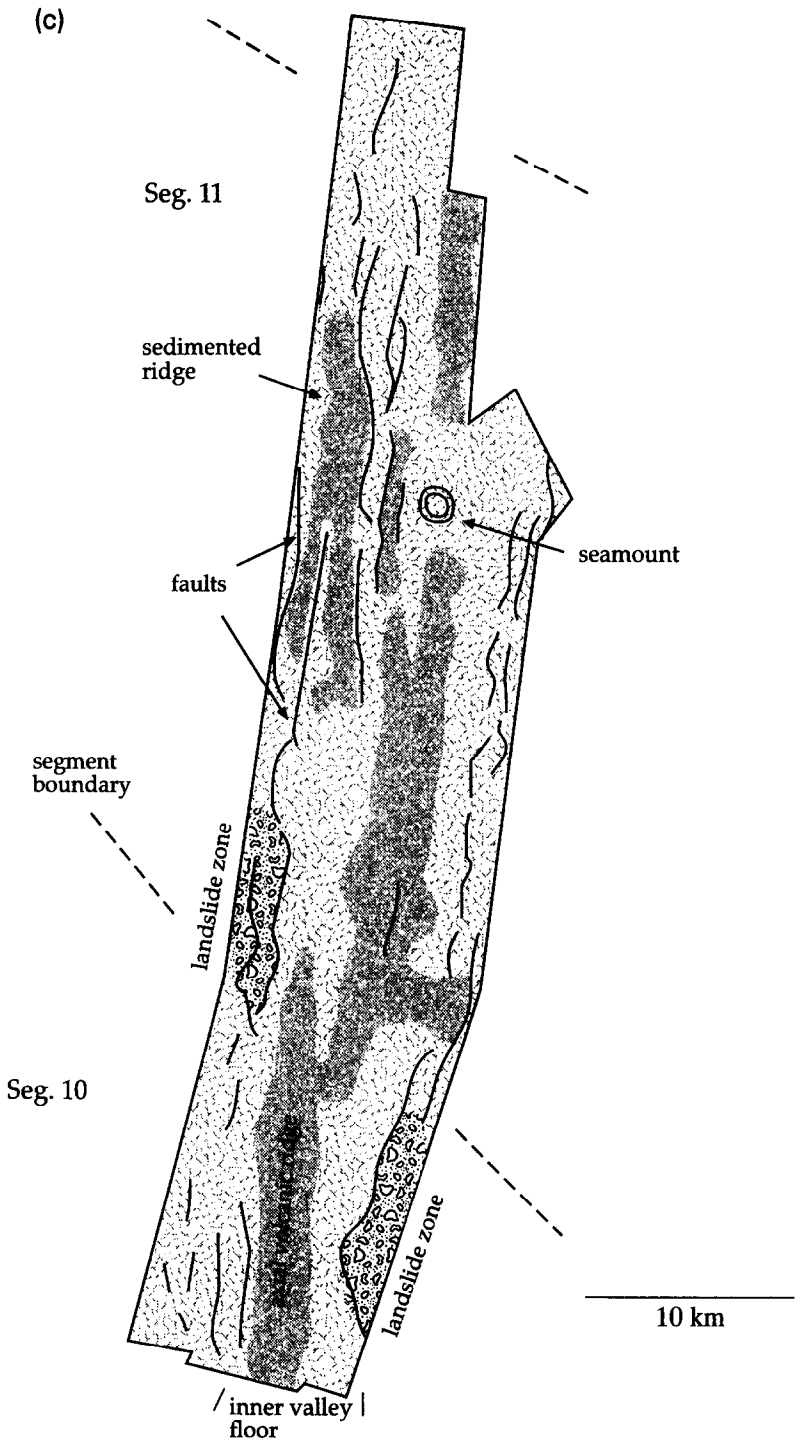
(c)
Seg. 11
sedimented ridge
faults
seamount
segment boundary
landslide zone
Seg. 10
landslide zone
10 km
inner valley floor

ment 17 has a seamount density of 110 per 10^3 km^2.

Segment 16 is a short, wide segment; it is approximately 15 km long and 15 km wide. A relatively weak, mantle Bouguer gravity anomaly low (approximately 7 mgal along-axis variation) is centered on Segment 16 (Lin et al., 1990). Multibeam data indicate that the inner valley floor contains 3 parallel and offset volcanic ridges; seamounts are associated with each. The density of seamounts, 76 per 10^3 km^2, is smaller than that of adjacent Segment 17.

3.2. Area 2

Study Area 2 contains Segment 11 and the northern half of Segment 10 (Fig. 3). The offset between Segments 10 and 11 is small —approximately 3 km, and the axial volcanic ridges of the two segments overlap by about 6 km (Spencer et al., 1992). Numerous small volcanoes are associated with the overlap zone.

Segment 11 is approximately 40 km long, and the width of the inner valley floor is, on average, 7.5 km. The bathymetry shallows approximately 600 m along the axis. Surface gravity data collected during our side-scan sonar surveys yield a negative mantle Bouguer anomaly near the center of the segment (approximately 15 mGal decrease from the segment end). An axial volcanic ridge runs most of the length of the segment; it widens and narrows and is discontinuous in places, and seamounts are scattered along it. In the northern half of Segment 11 a volcanic ridge located asymmetrically to the west on the valley floor appears to be faulted into several sections by the southwards extension of a bounding fault into the valley floor. The westernmost sections of the ridge are inferred to be covered with sediment because of the low echo amplitudes associated with them. Apparently eruptions in this region of the inner valley floor are infrequent. Seamounts more centrally located within the valley floor have been built to the east of this faulted volcanic ridge. One, a 70-m-high flat top volcano with a summit crater is labelled on the side-scan sonar mosaic in Fig. 3. It and other seamounts (not marked) fill the gap where the axial ridge is discontinuous. The density of seamounts in Segment 11 is 133 per 10^3 km^2, the highest of all the segments between the Kane and Atlantis transforms.

Segment 10 is approximately 45 km long; the inner valley floor is about 6 km wide. Segment 10 has an along-axis change in relief of ~750 m, and a negative mantle Bouguer anomaly near its center that is approximately 10 mGal less than at its ends. The axial volcanic ridge in Segment 10 is discontinuous near the midpoint of the segment. This gap marks the southern extent of the side-scan survey. On the eastern wall of Segment 10, a large landslide (Tucholke, 1991) has covered the bounding scarp and artificially narrowed the valley floor. The density of seamounts in Segment 10 is 67 per 10^3 km^2, approximately half that estimated for Segment 11.

Also of note in Area 2 is the Segment 10–11 boundary; there is no morphological evidence in the side-scan sonar that the 2 segments are distinct; nonetheless, gravity data show a mantle Bouguer anomaly low associated with both Segments 10 and 11 (Table 1) indicating that each is an individual spreading segment. Segmentation is also seen in the regular change in depth along the axis, shallowing near the center and deepening at the ends of each segment.

3.3. Area 3

Area 3 contains all but the northernmost part of Segment 6 and the western edge of Segment 5 (Fig. 4). The boundary between Segments 5 and 6 is complex. Using the TOBI data presented here to help interpret the Sea Beam bathymetry, Spencer et al. (1992) characterized the boundary as a shear zone that is composed of a region of oblique extensional faulting.

Segment 6 is about 55 km long, and has an average inner valley floor width of 7.5 km. The along-axis change in relief from segment end to center is ~750 m. A large negative mantle Bouguer anomaly, the largest associated with the spreading segments considered here, is located near the center of Segment 6 (about 22 mGal variation). Segment 6 is the only segment of the eighteen identified between the Kane and Atlantis transforms that contains no axial volcanic ridge. Instead it has a shallow (~150 m) central graben extending along much of its length with numerous isolated volcanic edifices scattered on the valley floor. These edifices are surrounded by extensive smooth-textured terrain. A transition to the more common (in our study areas) hummocky terrain occurs going southward along the segment. The density of seamounts in Segment 16 is 84 per 10^3 km^2, comparable to that of the other segments.

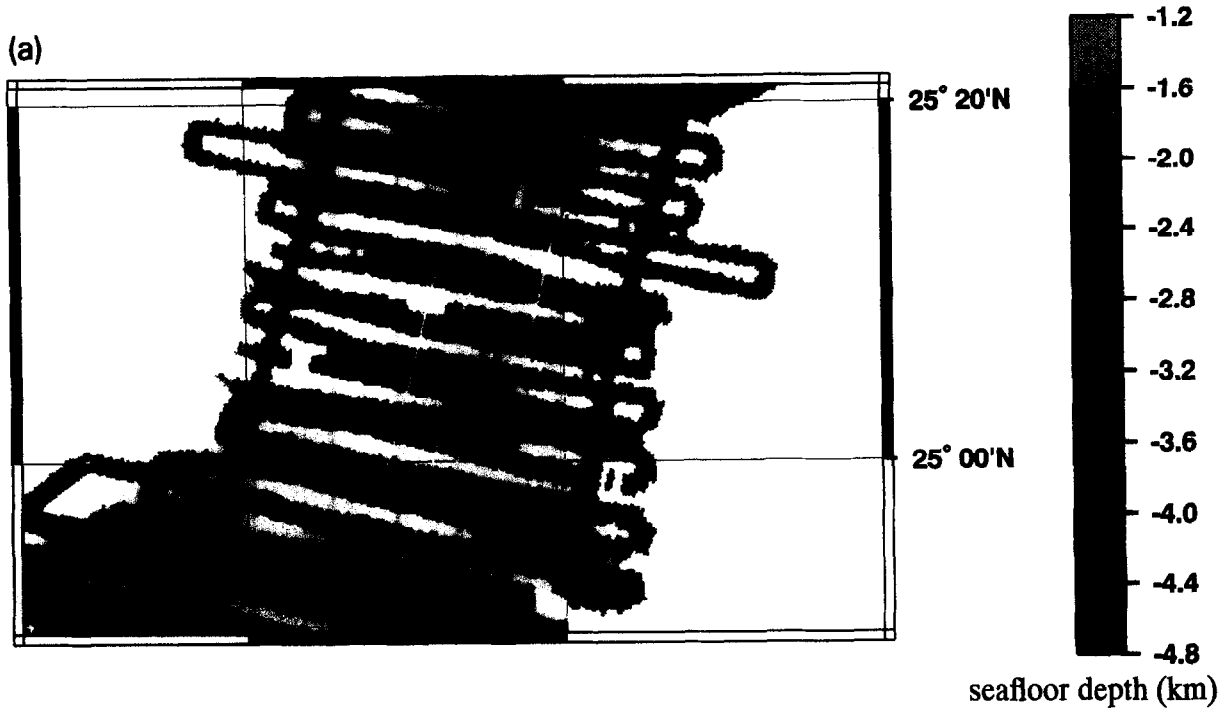

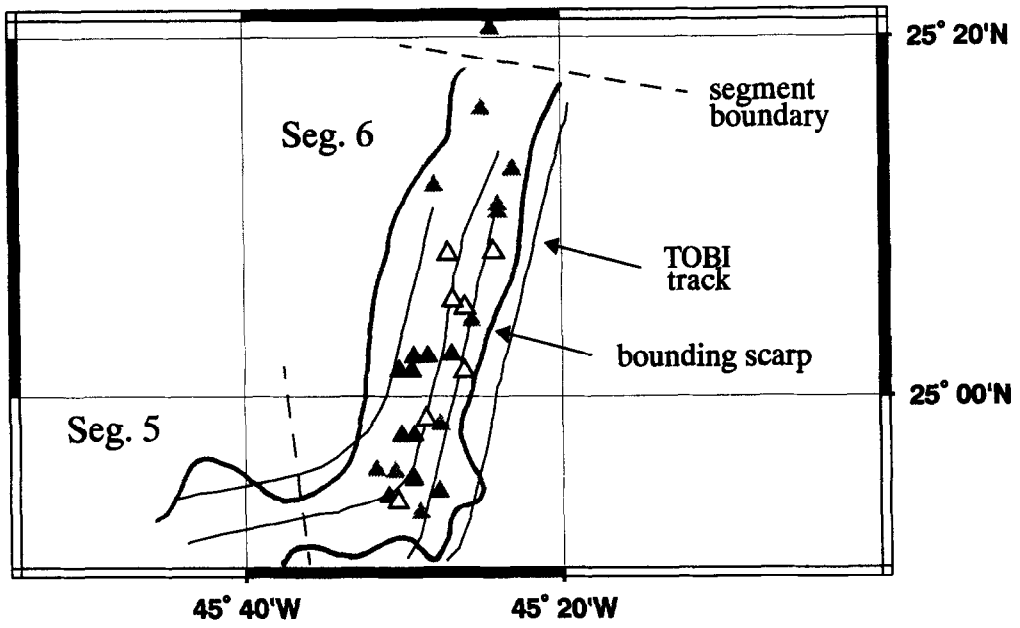

Fig. 4. Area 3 bathymetry (a), side-scan sonar data (b), and geologic interpretation (c). (a) Bathymetry and locations of identified seamounts are shown. See Fig. 2 for description of the data and shade coding of triangles. (b) Side-scan sonar mosaic of Area 3 composed of four overlapping swaths. See Fig. 2 for description of the data. Segment 6 has no axial volcanic ridge; instead a shallow graben (100–150 m deep) extends along its center; extensive smooth-textured terrain is observed here. Several small ridges aligned along the central graben are indicated and a detailed image of the northernmost one of these is shown in Fig. 11. Also marked are 3 hat seamounts that appear to be aligned along the strike of the segment. The southern two are shown in detail in Fig. 9c. The other seamount marked to the north of the hat seamounts has a hummocky texture and is shown in Fig. 7. The easternmost track is outside the valley floor and the lower backscatter returns are most likely caused by sediment buildup. (c) Geologic interpretation of the side-scan sonar mosaic in (b). The same features are marked on both.

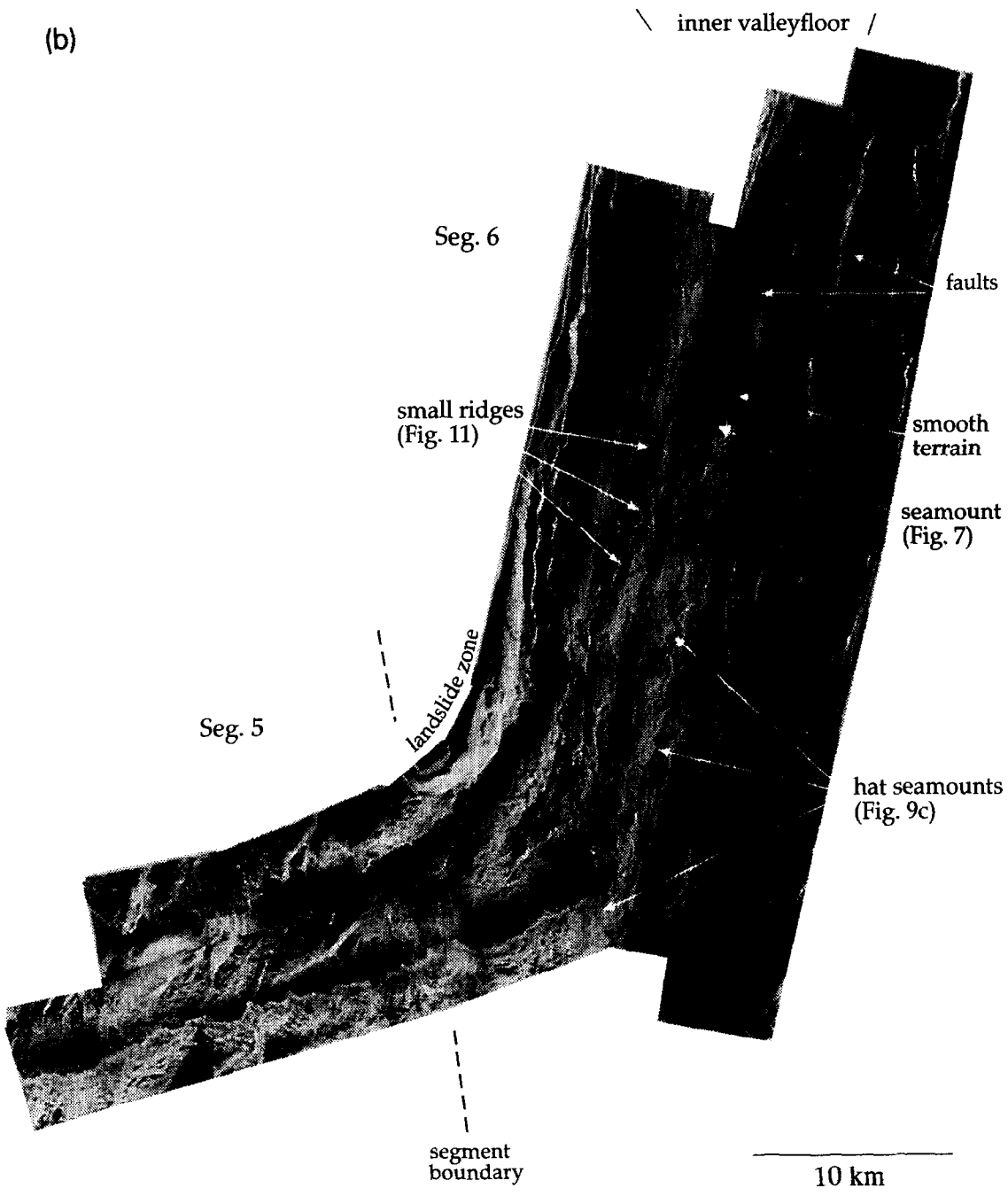

Fig. 4 (continued).

Segment 5 is the easternmost segment of a major zone of dextral offset of the MAR axis; its east–west dimension (~ 15 km) is longer than the north–south length (~ 11 km). Several short parallel ridges are observed in Segment 5 striking approximately parallel to the strike of the ridge axis (~ 010°). A 630-m-high edifice interpreted as a tilted fault block is located in the northwest section of this segment. Because of the

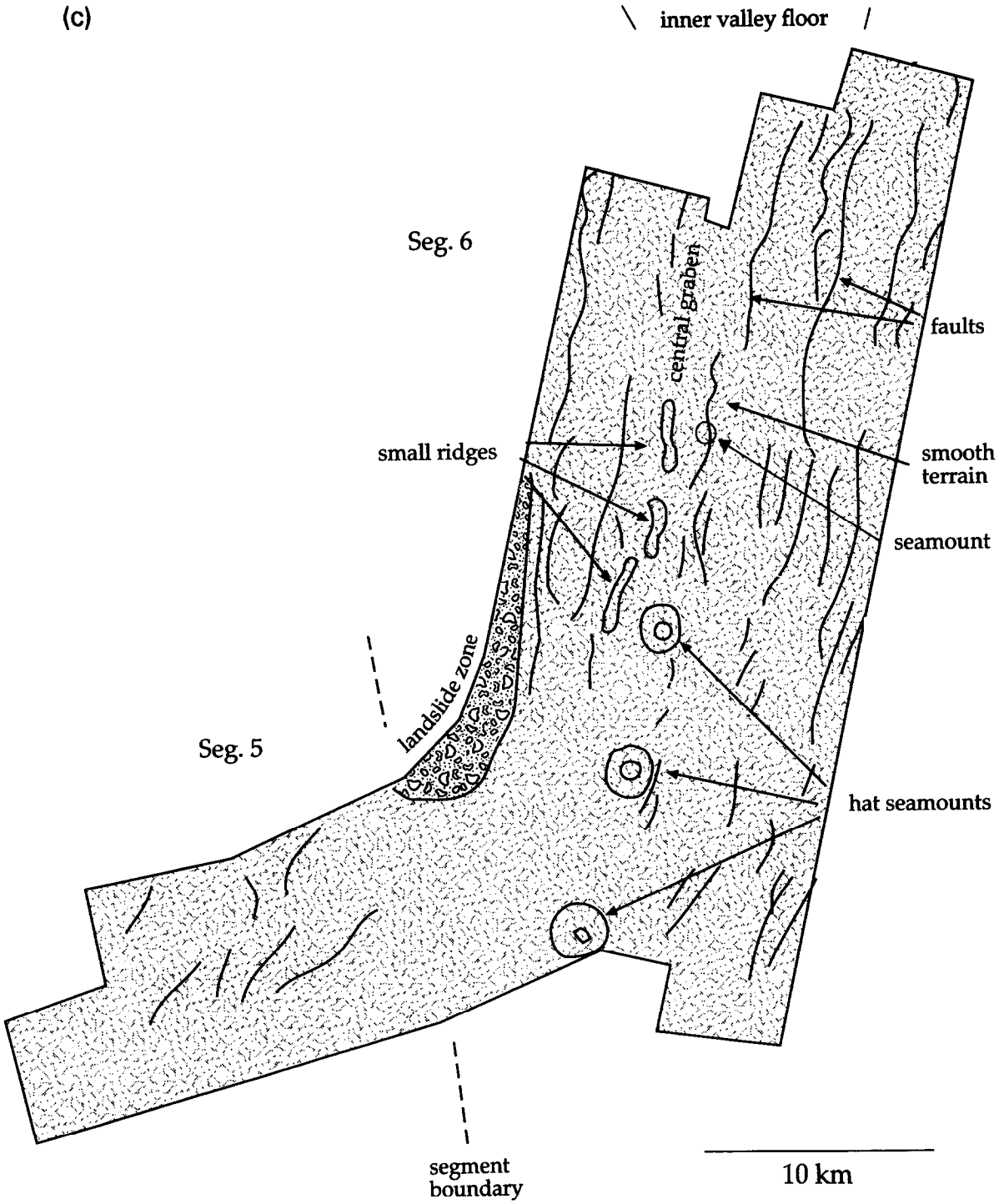

Fig. 4 (continued).

complicated structure of Segment 5 it is not considered further in this paper.

3.4. Area 4

Area 4 is located approximately 8 km north of Area 3, and is composed of Segment 7 and the southern two

thirds of Segment 8 (Fig. 5). The offset between Segments 7 and 8 is large (~ 10 km), and a septum separates the two (Spencer et al., 1992).

Segment 8 is approximately 42 km long, and has a wide inner valley floor —12 km, on average. Segment 8 has an along-axis change in relief of ~ 500 m, relatively small compared with those of the segments in the other 3 study areas, but the same as that of Segment 7 (see below). A negative mantle Bouguer anomaly (approximately 16 mGal variation along the axis) is located near the center of Segment 8. A large axial volcanic ridge approximately 3 km wide and 250 m high runs along much of the valley floor. The volcanoes built in Segment 8 have the largest average height (~ 135 m) of all of those of the eighteen segments between the Kane and Atlantis transforms. The two seamounts labelled on the side-scan sonar mosaic that occur on the axial volcanic ridge are 270 m (southern one) and 200 m in relief —essentially the same height as the volcanic ridge. The density of seamounts in Segment 8 determined from the multibeam bathymetry, 48 per 10^3 km^2, is the lowest (except for the short Segment 5) of the 18 segments between the Kane and Atlantis transforms.

Segment 7 is approximately 35 km long, and its inner valley floor is wide, averaging 10 km. Segment 7 has an along-axis change in relief of ~ 500 m. A weak negative mantle Bouguer anomaly (approximately 9 mGal variation —about half of that in Segment 8) is located south of the center of Segment 7. The inner valley floor of Segment 7 is dominated by a robust axial volcanic ridge that is approximately 3 km wide, and runs most of the length of the segment. Its height of about 500 m is twice that of the volcanic ridge in Segment 8. Volcanoes are scattered along the top and sides of the axial volcanic ridge. A morphologically diverse group of volcanic features is observed in the western flanking deep of the axial volcanic ridge. The group consists of an approximately 120-m-high flat top seamount, small volcanic ridges extending to the north and south, and a smooth-textured patch between the two ridges to the south. The density of seamounts in Segment 7 is 88 per 10^3 km^2, nearly twice that estimated for Segment 8. The westernmost TOBI track in Area 4 is located outside the inner valley floor, and imaged a sedimented volcanic ridge on the step of the first fault block in the median valley wall that is inferred to be a fossil axial volcanic ridge.

4. Seamount population parameters

In the following we describe the parameters of the seamount population in our four study areas estimated from the bathymetry data. The criteria used by Smith and Cann (1990, 1992) to include a feature in their seamount counts were that the feature had to be an edifice with height $h \geq 50$ m and near-circular in plan shape. The lower cutoff height ($h = 50$ m) is based on the resolution of the multibeam data. In the four study areas a total of 146 seamounts were identified by Smith and Cann (1992); their locations in each area are shown below the bathymetry maps in Figs. 2–5. The size distribution and shape parameters of these seamounts are given here and compared to those of the entire population between the Kane and Atlantis transforms (481 seamounts).

The parameters useful in describing and comparing seamount populations include characteristic summit height, β^{-1} (Smith and Jordan, 1988), height-to-diameter ratio, ξ_d, and flatness, f, this being the ratio of top diameter to bottom diameter. The values of summit height, and basal and summit diameters, used to estimate these parameters have been measured previously

Fig. 5. Area 4 bathymetry (a), side-scan sonar data (b), and geologic interpretation (c). (a) Bathymetry and locations of identified seamounts are shown. See Fig. 2 for description of the data and shade coding of triangles. (b) Side-scan sonar mosaic of Area 2 composed of three overlapping swaths. See Fig. 2 for description of the data. The eastern half of the inner valley floor of Segment 7 was not imaged. Instead a TOBI track was run outside the valley floor to the west. A sedimented ridge was imaged on the first fault block of the bounding wall. This ridge is inferred to be a fossil axial volcanic ridge. A smooth flat top seamount is marked to the west of the axial volcanic ridge in Segment 7; it is associated with several small ridges, and a smooth patch occurs to its south. A detailed image of this seamount is presented in Fig. 9b. Also marked in Segment 7 is a small volcanic ridge that has been built on the western flank of the axial volcanic ridge. It is shown in Fig. 11. In Segment 8, two hummocky seamounts are labelled. These types of seamounts are the most common in our study areas. The southern one is shown in Fig. 7. (c) Geologic interpretation of the side-scan sonar mosaic in (b). The same features are marked on both. In addition, the approximate location of the axial volcanic ridge is shaded.

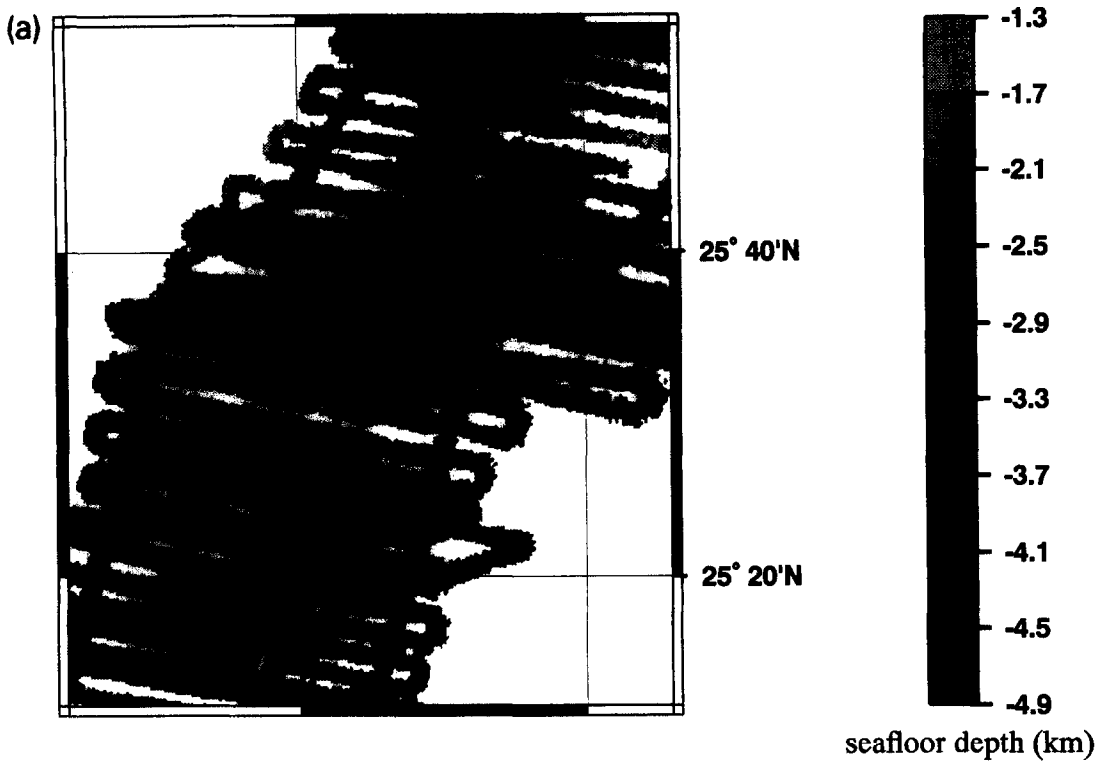
(a)
25° 40'N
25° 20'N
-1.3
-1.7
-2.1
-2.5
-2.9
-3.3
-3.7
-4.1
-4.5
-4.9
seafloor depth (km)

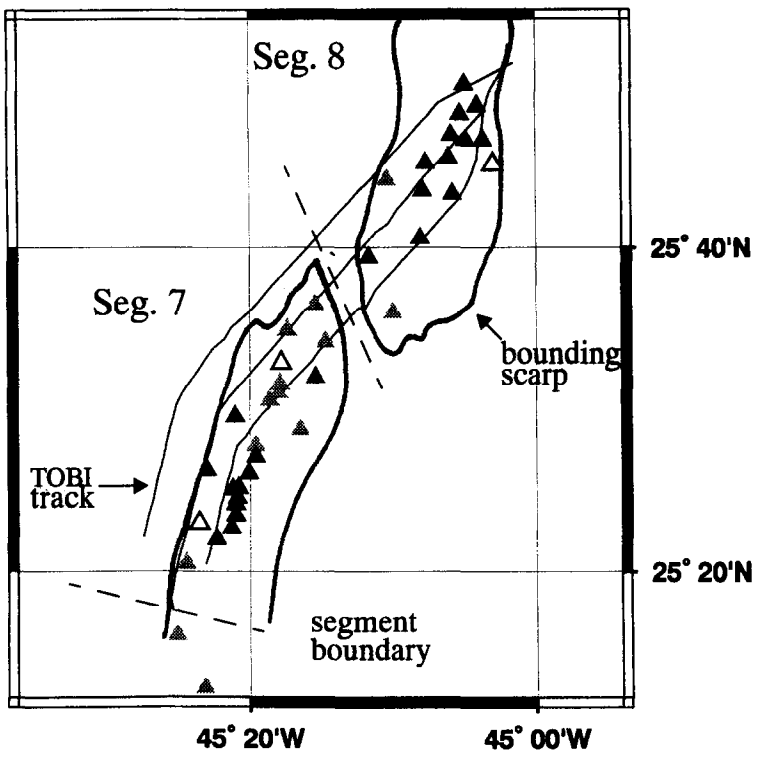
Seg. 8
Seg. 7
25° 40'N
bounding scarp
TOBI track
25° 20'N
segment boundary
45° 20'W
45° 00'W

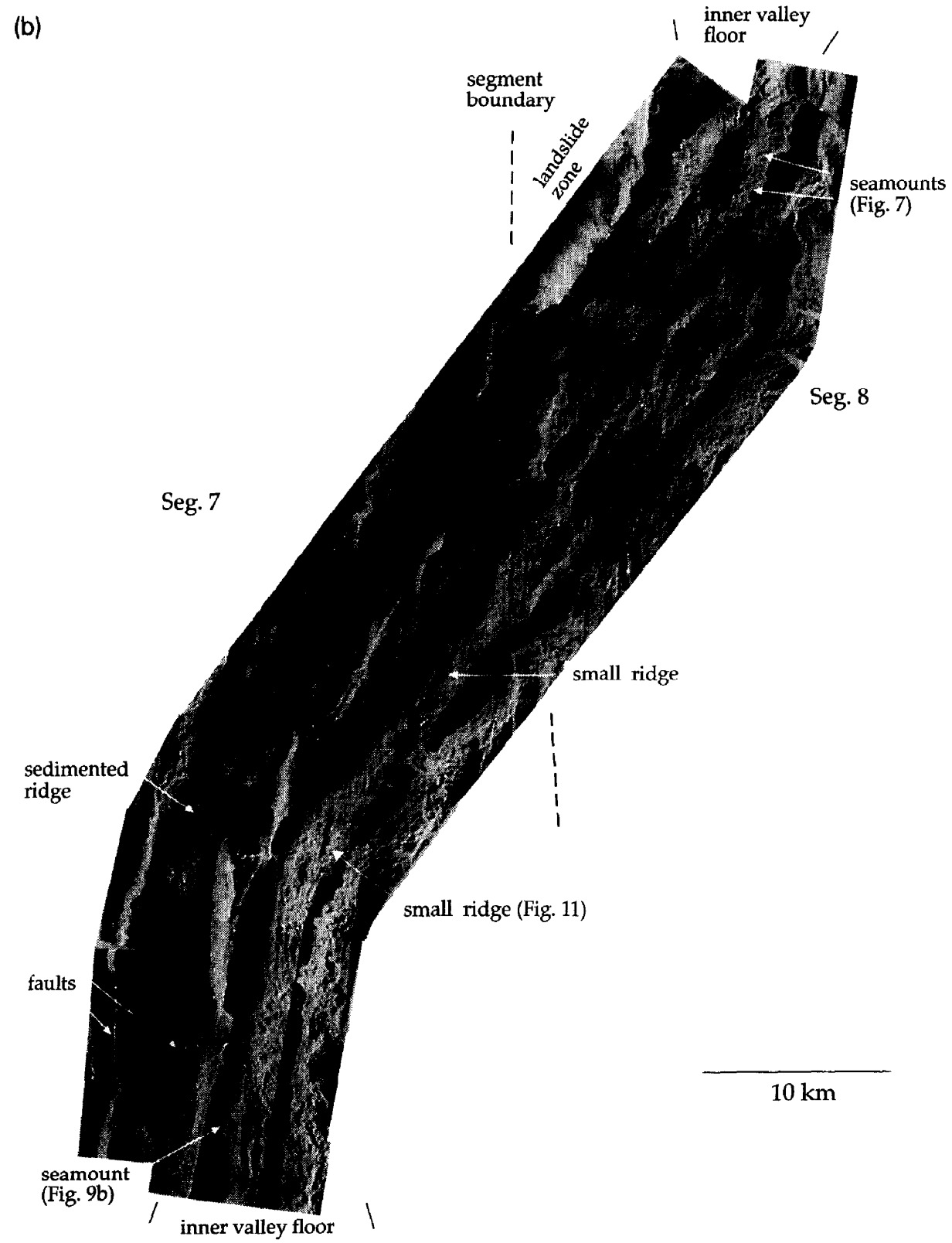
(b)
inner valley floor
segment boundary
landslide zone
seamounts (Fig. 7)
Seg. 8
Seg. 7
small ridge
sedimented ridge
small ridge (Fig. 11)
faults
10 km
seamount (Fig. 9b)
inner valley floor

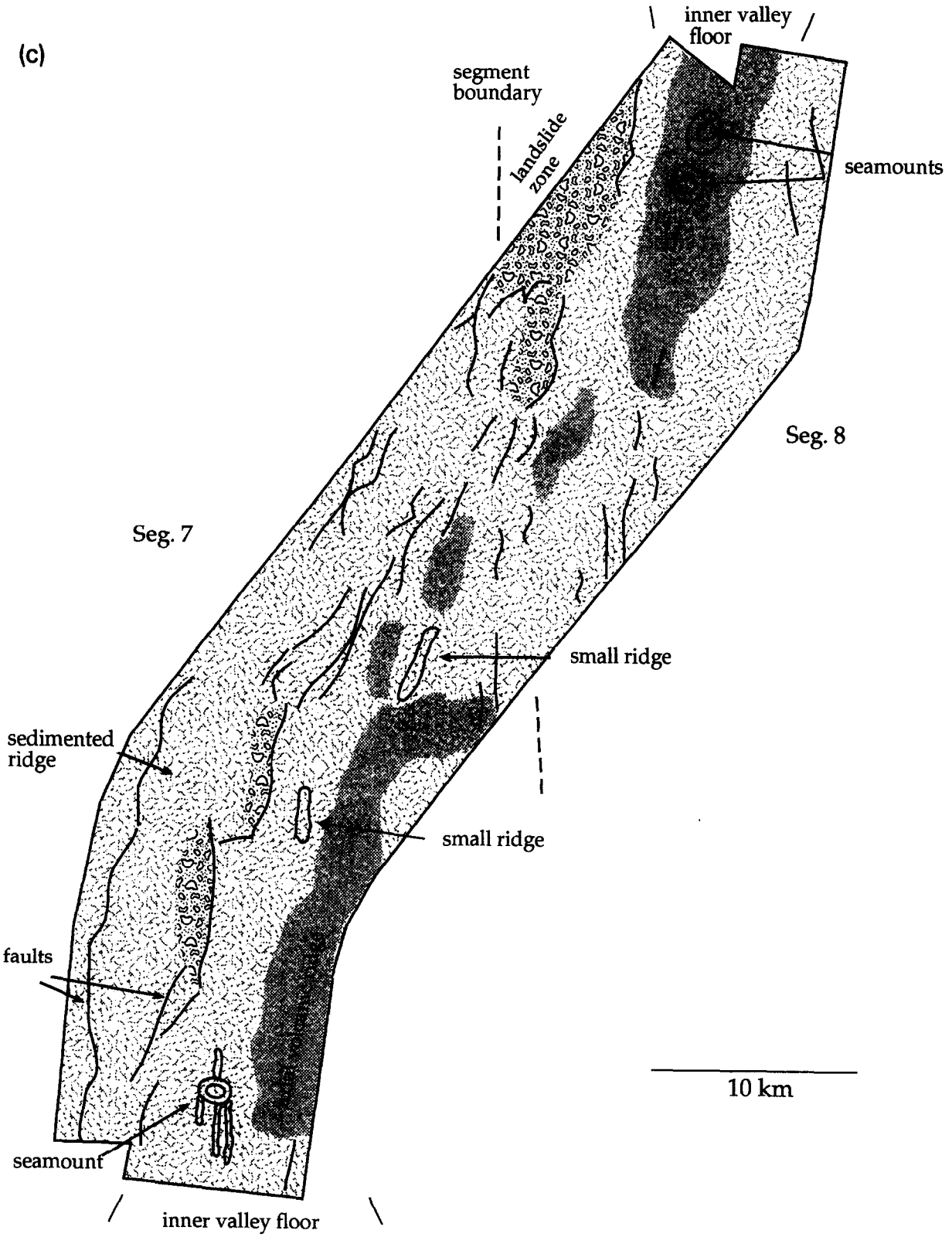

Fig. 5 (continued).

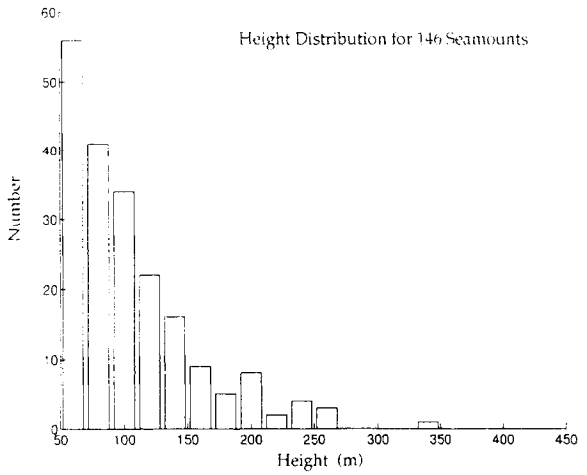

Fig. 6. Height distribution for the 146 seamounts identified in the four study regions by Smith and Cann (1992) from multibeam bathymetry. Heights have been sorted into 20-m bins. The observed fall-off of number with height is consistent with the exponential size-frequency model of Jordan et al. (1983).

from the bathymetry data by Smith and Cann (1990, 1992). The distribution of 146 summit heights displayed in Fig. 6 shows that the number of seamounts decreases exponentially with increasing height. A maximum likelihood fit of an exponential function (Smith and Jordan, 1988) to the binned data in the height range 50–210 m (bin counts ≥ 5) yields a characteristic summit height of $\beta^{-1} = 63 \pm 3$ m, essentially the same as that obtained for the entire population ($\beta^{-1} = 58 \pm 2$ m).

The 146-point sample mean for height-to-diameter ratio is $\xi_d = 0.11 \pm 0.03$ implying that the diameter of a seamount is on average just more than 10 times its summit height. The mean value of ξ_d is consistent with that determined by Smith and Cann (reported as height-to-radius ratio, $\xi_r = 0.21 \pm 0.06$) as well as by other studies that have compiled seamount shape statistics in both the Pacific and Atlantic oceans (e.g., Batiza and Vanko, 1983; Abers et al., 1988; Smith, 1988; Kong et al., 1988). Flatness varies from 0 (pointy cone) to 0.7 (flat top cone) and shows no clear relationship with height. The 146-point sample mean is $f = 0.30 \pm 0.16$. This is the same range and mean value for flatness obtained for the whole population (0–0.7, $f = 0.31 \pm 016$).

Based on the similarities in population and shape parameters we conclude that the 146 seamounts located in our four study areas are representative of the entire population between the Kane and Atlantis transforms.

5. Morphological types of seamounts

Using bathymetric overlays we located 109 of the 146 seamounts in the side-scan sonar images (Table 3). Despite attempts to survey the entire floor, some of the seamounts ended up directly beneath the vehicle path, and therefore were not imaged. The volcanic morphologies of the 109 seamounts as seen in the side-scan sonar images are striking, and not evident in the multibeam data. Although the resolution of the side-scan sonar is not good enough to discriminate between individual flow morphologies such as those of sheet flows and pillow basalts, two distinct seamount surface textures are evident on the scale of tens of meters: hummocky (bulbous), and smooth. (The word hum-

Table 3
Classification of the morphological types of seamounts

Study area	Segment	Seamount counts		Classification by surface morphology	
		Bathymetry	Side-scan sonar	Hummocky seamounts	Smooth seamounts
1	17	23	17	14	3
	16	11	9	9	0
2	11	38	31	27	4
	10	9	8	6	2
3	6	26	17	10	7
4	8	15	13	12	1
	7	24	14	12	2
Total		146	109	90	19

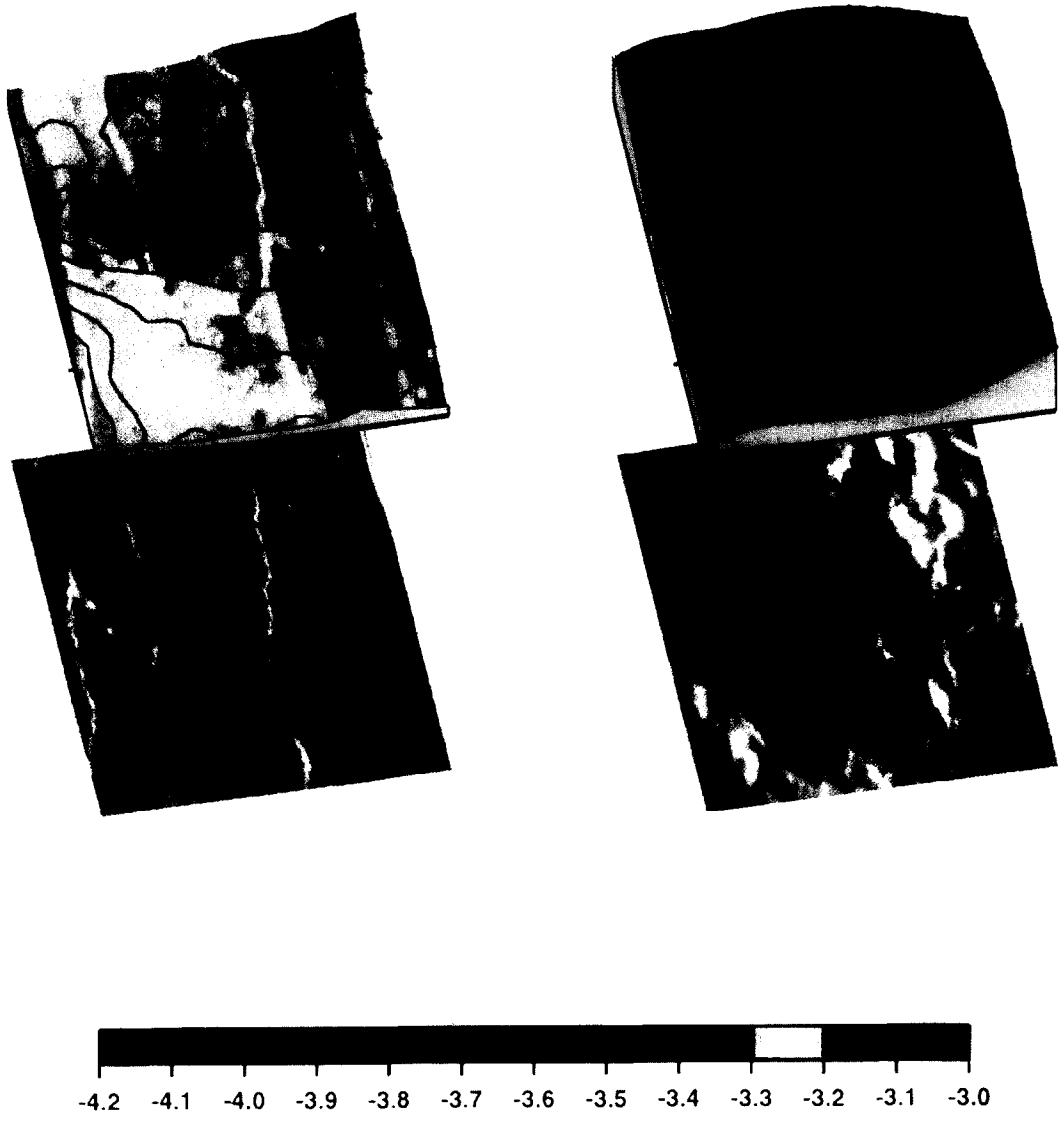

Fig. 7. Two examples of hummocky seamounts. Multibeam bathymetry data are shown above the side-scan sonar image. The bathymetry data have been extracted from a gridded data set using latitudes and longitudes corresponding to the estimated position of the TOBI vehicle. These two data sets are not co-registered, however. Color corresponds to water depth, and 20-m contour intervals have been plotted. The bathymetry has been shaded using the intensities of the side-scan sonar data, and not the topographic gradient. Therefore, the side-scan "textures" can be seen on the bathymetry maps. Each figure is the same size, ~2.5 km along the bottom and ~3.25 km along the side. The left panel presents a hummocky seamount located in the central graben of Segment 6 (Fig. 4); it is surrounded by smooth-textured terrain, and faults cut its flank. Its summit is located in a gap in the bathymetry data so that the contours running east–west from the summit are artifacts of the gridding program. Extrapolating from contours of only the northern flank of the seamount, we estimate it to be ~100 m in relief. It is built from numerous hummocks, with diameters of a few tens of meters, piling on top of each other. The right panel shows the southern hummocky seamount located at the top of the axial volcanic ridge in Segment 8 of Area 4 (Fig. 6). These types of hummocky seamounts located on the tops and sides of axial volcanic ridges are very common in our study regions. This one is approximately 270 m high, with basal diameter of ~2225 m.

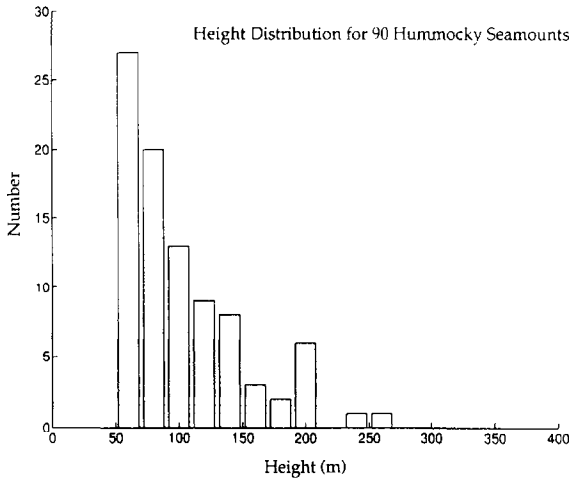

Fig. 8. Height distribution for the 90 hummocky seamounts identified in the four study regions from the side-scan sonar data. Heights have been sorted into 20-m bins. The observed fall-off of number with height is consistent with the exponential size-frequency model of Jordan et al. (1983), and similar to that observed for the population of 146 seamounts shown in Fig. 6.

mock is used here to describe rounded mounds 50–500 m in diameter and less than 50 m high.) The spatial locations of the different morphological types of seamounts are shown in Figs. 2–5. Examples of hummocky-and smooth-textured seamounts are shown below.

5.1. Hummocky seamounts

A hummocky seamount has a bulbous morphology. Hummocky seamounts dominate in our study areas: 83% of the seamounts identified in the TOBI side-scan sonar images have hummocky morphologies (Table 3). Detailed images of two hummocky seamounts are presented in Fig. 7 along with the corresponding bathymetry data. The format of this figure is the same as that in the following several figures, and we describe it here. Bathymetry data are shown above the side-scan sonar images. The bathymetry data have been extracted from a larger gridded data set using latitudes and longitudes corresponding to the estimated position of the TOBI vehicle. These two data sets are not co-registered, however, and matching the two is often subjective. Color corresponds to water depth, and 20-m contours have been plotted. The bathymetry has been shaded using the intensities from the side-scan sonar data; thus, the side-scan textures can be seen "through" the bathymetry. Each plot shows a patch of seafloor approximately 2.5 km wide and approximately 3.25 km long. The left panel in Fig. 7 shows a hummocky seamount located in the central graben of Segment 6 (Fig. 4) surrounded by smooth-textured terrain; faults cut its flank. The right panel shows the southern hummocky seamount located at the top of the axial volcanic ridge in Segment 8 of Area 4 (Fig. 6). Hummocky seamounts associated with axial volcanic ridges are the most common type of seamount in the study areas.

Hummocky seamounts range in height between 50 and 270 m (Fig. 8). The characteristic height of the 90 hummocky seamounts (from a maximum likelihood fit to the binned data between the heights 50 and 210 m) is $\beta^{-1} = 62 \pm 3$ m. The 90-point sample mean for height-to-diameter ratio is $\xi_d = 0.11 \pm 0.03$. Flatness varies from 0 to 0.63; the sample mean is $f = 0.29 \pm 0.15$. The size and shape parameters describing the hummocky seamounts do not vary significantly from those estimated for the 146 seamounts located in the study regions

The spatial distribution of hummocky seamounts on the inner valley floor of the study areas is shown in Figs. 2–5. All hummocky seamounts are associated with the larger axial volcanic ridges in Study Areas 1, 2, and 4. In Area 3, where there is no volcanic ridge, hummocky seamounts are more common in the southern half of Segment 6.

5.2. Smooth seamounts

Volcanoes with smooth surface morphology on the side-scan sonar images are classified as smooth seamounts; they make up approximately 17% of the seamount population (Table 3). Detailed images of smooth seamounts are presented in Fig. 9. We categorize smooth seamounts into two groups: flat top seamounts and hat seamounts. Fig. 9a presents detailed images of large flat top seamounts; Fig. 9b presents detailed images of small flat top seamounts, and Fig. 9c detailed images of hat seamounts.

Both seamounts shown in Fig. 9a are located in Study Area 1 (Fig. 2). The 220-m-high seamount presented in the left panel of Fig. 9a has a summit crater that makes up most of the flat top which has been cut by faults. A graben has formed on the summit, and down-dropped blocks are observed on each side of the

crater. Hummocks cover much of the flanks. The right panel shows a tall seamount (~350 m in relief) situated at the southern terminus of the axial volcanic ridge in Segment 17. Its flat top contains a shallow crater. Numerous faults cut its flanks, and hummocks cover parts of the summit and flanks. A ridge has built on its southeast flank.

The smooth flat top seamount shown in the left panel of Fig. 9b is approximately 70 m high, and is located in Area 2 (Fig. 3). The flat top is not faulted, and therefore it may have been recently constructed. The keyhole shape of the shallow summit crater suggests that two adjacent craters have coalesced. Hummocks have formed on the flanks of the seamount and within the crater. The smooth flat top seamount shown in the right panel is approximately 120 m high, and is located at the southern end of Area 4. As seen in Fig. 5, it is part of a morphologically diverse group of volcanic features that includes small ridges and a region of smooth-textured terrain. Its flat top is cut by faults, two of which have formed a small down-dropped graben.

The second category of smooth seamount is characterized by a central edifice surrounded by axisymmetric flows. The smooth-textured brim has led to the use of the term "hat seamount" to describe these distinctive seamounts. Only 3 of the 109 seamounts are hat seamounts; two of these are located in the central graben of Segment 6 in Study Area 3 (Fig. 4). The other is located in the flanking deep east of the large axial volcanic ridge in Segment 8. Fig. 9c shows examples of two hat seamounts, both from Segment 6. A few other hat seamounts have been identified in the side-scan sonar data; these, however, are not included in the seamount counts because they are unfortunately located in gaps in the bathymetry data.

The height distribution of the 19 smooth seamounts is shown in Fig. 10. The small sample size makes it impossible to estimate a characteristic summit height for the population of smooth seamounts. The 19-point sample mean for height-to-diameter ratio is $\xi_d = 0.11 \pm 0.04$. Unlike hummocky seamounts, smooth flat top seamounts show a relationship between height-to-diameter ratio and summit height. That is, ξ_h increases nearly linearly with increasing h. The height-to-diameter ratios ξ_d of the three hat seamounts are smaller than average, suggesting that the growth of hats occurs radially more than upwards compared to other types. The flatness of all smooth seamounts varies from 0.13 to 0.69; the 19-point sample mean is $f = 0.32 \pm 0.17$. Although the mean flatness is slightly larger than that obtained for hummocky seamounts, the binned flatnesses are not well approximated by a gaussian distribution, and show a large peak at $0.1 \leq f \leq 0.2$.

The spatial distribution of smooth seamounts is shown for each of the study areas in Figs. 2–5. Smooth seamounts are associated with axial volcanic ridges. They also occur, however, as isolated features. For example, the cratered smooth seamount in the left panel of Fig. 9b is located in a gap in the axial volcanic ridge in Segment 11; the smooth seamount shown in the right hand panel of Fig. 9b is located in the flanking deep to the west of the axial volcanic ridge in Segment 7 (Fig. 6).

The images in Fig. 9 reveal that smooth seamounts often have hummocks on their flanks and summits. How these hummocks relate to the seamounts is not clear. They may form at the end of the building stage and cover the flanks and fill the summit crater. Alternatively, hummocks may be unrelated to the eruptions that build the seamount. Despite the fact that hummocks cover parts of smooth seamounts, smooth seamounts can always be distinguished from hummocky seamounts by their remarkably flat tops (sometimes with summit craters), and/or mostly smooth textured appearance on the TOBI images.

5.3. *Correlations between seamount morphology and segment properties*

To obtain a better understanding of the controls on seamount formation, we have investigated the variation in seamount morphology between and within segments. We find that Segment 6 with its extensive smooth-textured terrain, no axial volcanic ridge, and large negative mantle Bouguer anomaly has the highest percentage of smooth flat top and hat seamounts (41%). We are not sure what the connection between these parameters is, however. Large negative mantle Bouguer anomalies are generally associated with higher mantle temperatures or thicker crust or both (e.g., Kuo and Forsyth, 1988; Lin et al., 1990). It is possible that higher mantle temperatures, producing greater extents of partial melting and perhaps larger volumes of magma to the ridge, may have resulted in recent flooding of the inner valley floor of Segment 6 generating the smooth-textured terrain that is evident

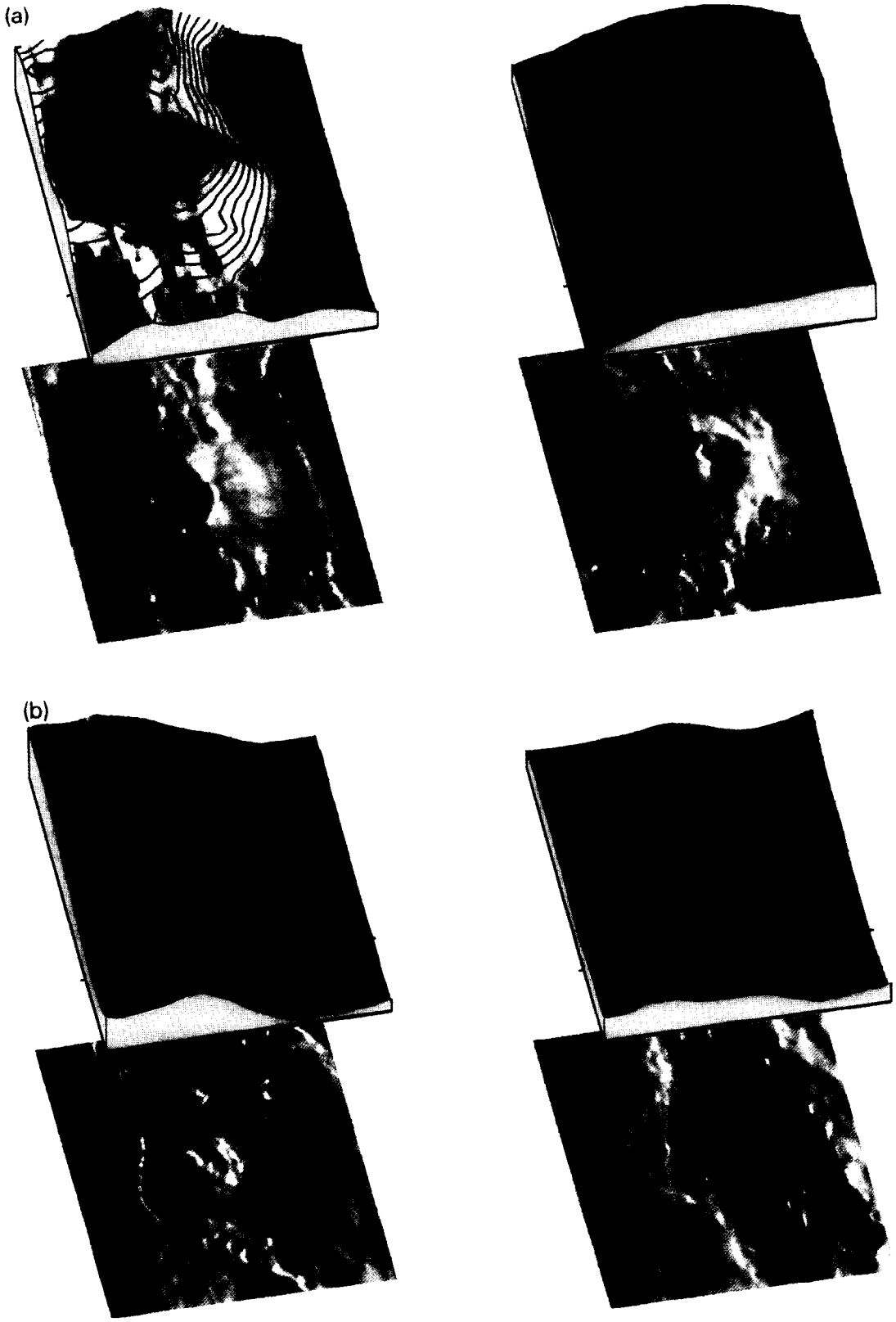
(a)
(b)

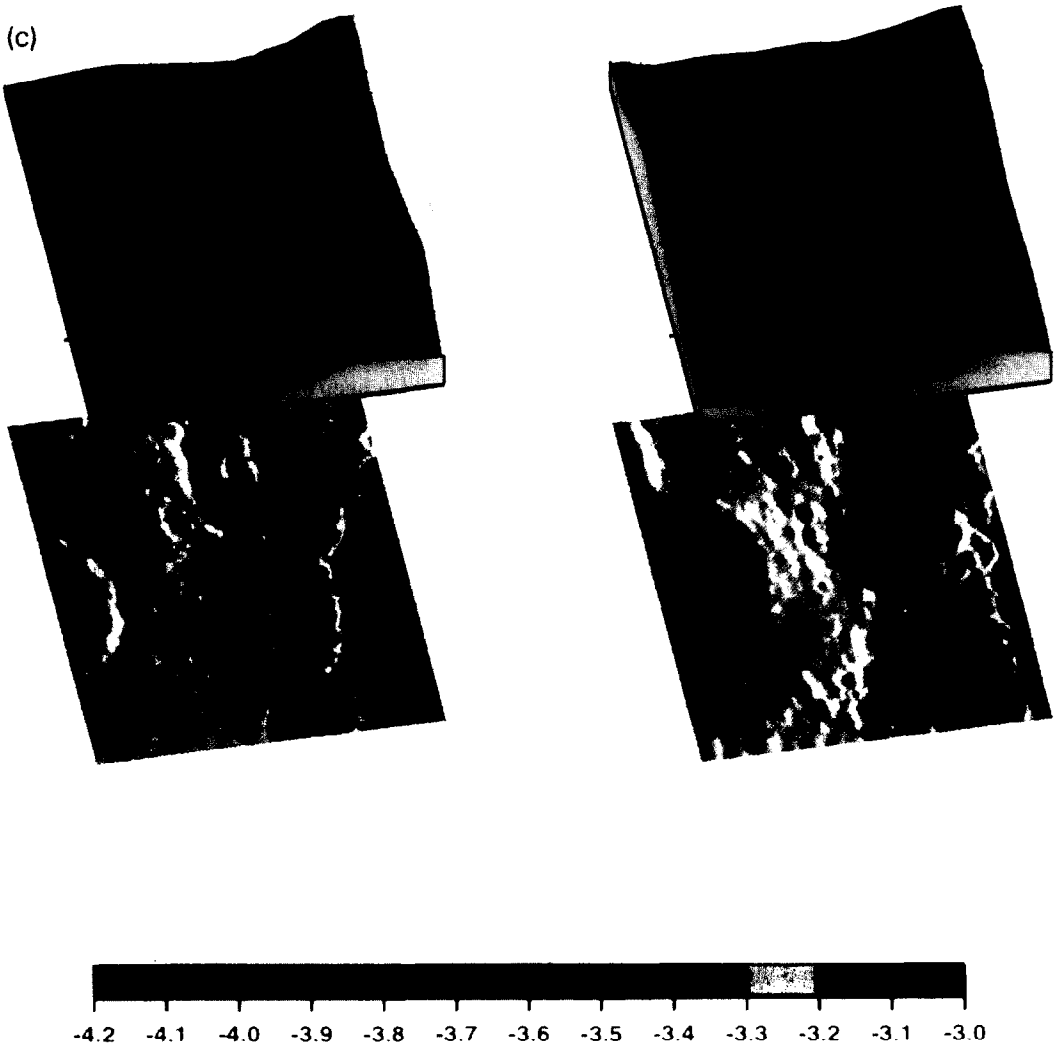

Fig. 9. Examples of smooth seamounts. The format of this figure is described in Fig. 7. (a) Tall, flat top seamounts. Both are located in Segment 17 of Area 1. The left panel shows a cratered seamount; it is ~220 m in relief with a basal diameter of ~1500 m and a summit diameter of ~600 m, most of which is taken up by the crater. The summit is cut by faults and fissures, and down-dropped blocks are observed on each side of the crater. Hummocks cover its flanks. The right panel shows the tallest seamount identified by Smith and Cann (1992). It is ~350 m in relief with a basal diameter of ~2200 m and summit diameter of ~600 m. Numerous faults cut its flanks, and hummocks cover parts of the flanks and summit. A shallow graben is observed at the summit. (b) Short, flat top seamounts. The seamount shown in the left panel is located in Segment 11 of Area 2. It has a summit height of ~70 m, a basal diameter of ~1600 m, and a summit diameter of ~1100 m. The summit crater appears to be filled with hummocks. Hummocks also occur at the edges of the flat top. The seamount shown in the right panel is located in Segment 7 of Area 4. It has a summit height of ~120 m, a basal diameter of ~1350 m, and a summit diameter of ~625 m. Small ridges extend to the north and south of this features, and it is possible that the seamount was built when an original fissure eruption collapsed to a single feeder. The top is faulted and a down-dropped block has formed on its western side. A smooth textured patch occurs between two of the ridges to the south. (c) Hat seamounts. Both are located in Segment 6 of Area 3. In the left panel the central dome of the feature is at the left of the image, only half of the edifice is shown. The dome is encircled by a smooth-textured brim. The summit height of the entire feature is ~80 m, the basal diameter ~2100 m, and the diameter of the central edifice is ~600 m. A taller hat seamount is shown in the right panel. It has a summit height of ~200 m, a basal diameter of ~1875 m, and a summit diameter of ~800 m. Its smooth surface is dotted with hummocks.

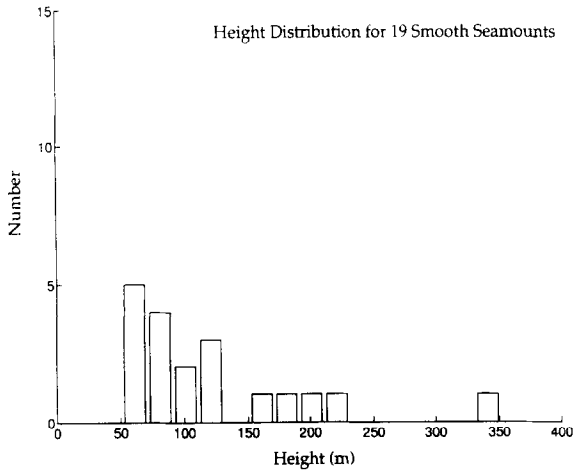

Fig. 10. Height distribution for the 19 smooth seamounts identified in the four study regions from the side-scan sonar data. Heights have been sorted into 20-m bins. There are too few smooth seamounts to constrain their size–frequency distribution. Their sizes span the entire size range observed for the 146 seamounts, 50–350 m.

there. The volcanic edifices isolated within this smooth-textured terrain may have been built prior to this episode or may be building on top of the smooth terrain; it is impossible to tell from the topography alone. No other systematic relationships between seamount morphology and segment properties (e.g., length, width, seamount density) have been found in any of the study areas.

Intrasegment variations in seamount morphology have also been investigated. Our results show that all hummocky seamounts are associated with axial volcanic ridges (Study Areas 1, 2, and 4) and occur on their tops and flanks. Smooth seamounts are also associated with axial volcanic ridges; however, most of them occur on the ridge flanks. In addition some smooth seamounts are observed in the flanking deeps, and others fill in the gaps in axial volcanic ridges. The one hat seamount not in Segment 6 is located in the flanking deep east of the axial ridge in Segment 8. (We assume that seamounts located in the flanking deeps of the axial ridges have formed there since they are not highly faulted and fractured as might be expected if they had been transported laterally from a more central location.) All hat seamounts, and all flat top seamounts that occur in topographic lows in Study Areas 1, 2, and 4, have lower than average height-to-diameter ratios, ξ_d, suggesting that their growth occurs preferentially outwards at their base rather than upwards. Correlations between seamount morphology and other variables such as location with respect to the bounding scarps or ends of segments have not been found.

6. Small volcanic ridges

In addition to nearly circular volcanic edifices, small (1–2 km in length) volcanic ridges are abundant on the inner valley floor of the MAR in our study regions. They are, in general, not evident in the bathymetry data. In Areas 1, 2 and 4 they occur on the tops and sides of the large axial volcanic ridges, as well as the flanking deeps. They are also numerous in Study Area 3, in some places well defined by the surrounding smooth-textured terrain. Commonly, the small ridges are aligned parallel to or subparallel to the strike of the segment. Occasionally, however, their strike is transverse to that of the ridge segment. Often, these small ridges are composed of individual mounds of comparable size suggesting that each mound represents a centralized eruption. In other places, the ridges are smoother and individual mounds are not as easily distinguished.

Fig. 11 presents two examples of small volcanic ridges. "Tadpole Ridge" shown in the left panel of Fig. 11 is located in Area 3 (Fig. 4). It is one of several volcanic ridges that are aligned along the shallow central graben in Segment 6. It sits in a background of smooth-textured terrain. The orientation of Tadpole Ridge mimics the orientation of neighboring faults and fissures, and it is inferred that the feature was built by eruptions through similar faults and fissures. Its height is about 30 m, on average; a near-circular volcano (40–50 m in relief) is located at the southern end of the ridge; a smooth-textured brim surrounds it.

"Caterpillar Ridge" shown in the right panel of Fig. 11 is located on the western flank of the axial volcanic ridge in Segment 7 (Fig. 5). It is not well defined in the bathymetry data. It appears to be composed along its length of individual, roughly circular mounds. Ridges such as this one may form from a fissure eruption in a manner similar to those observed in Iceland and Hawaii in which the original eruption breaks down to several points along the fissure to build ridges composed of a string of discrete highs.

7. MAR volcanoes – modes of formation

The side-scan sonar data presented in this paper provide high-resolution images of the many volcanic edifices built on the inner valley floor of the MAR between 25° and 29°N. An analysis of these data shows that seamounts 50–350 m in relief are fundamental building blocks of the segment-scale topography. They have distinct volcanic morphologies and shapes and, in combination with small ridges and fields of hummocks, assemble themselves into large axial volcanic ridges. Understanding the formation of these seamounts and their relationship to the axial volcanic ridges is critical to understanding how the shallow crust is constructed at a slow-spreading ridge.

Possible analogs to the hummocky-and smooth-textured MAR edifices have been mapped in the Troodos ophiolite in Cyprus, and are called "pillow" and "sheet" volcanoes by Schmincke and Bednarz (1990). Pillow volcanoes are composed of pillows of varying diameters (up to 6 m) and are thought to result from low-viscosity lavas that erupted at steady slow rates to build upward-growing bulbous masses. Sheet volcanoes are composed of discrete low-relief flows typically less than 5 m thick and are associated with more intermediate lavas, fast eruption rates, and distinct eruptive events. Schmincke and Bednarz (1990) concluded from their study that the composition of the lava is not the most important factor governing the formation of pillow or sheet volcanoes. Formation is largely related to mass eruption rate and volume of lava erupted.

Laboratory simulations of volcano growth using hot wax extruded under water also indicate that slow eruption rates and/or rapid cooling of the lava surface produce features that build by individual bulbous outgrowths; smooth-textured edifices form when eruption rates are high, or cooling of the lava surface is slow (e.g., Griffiths and Fink, 1993). In addition, laboratory models indicate that the shapes of edifices will vary. Fast eruption rates will build edifices with low aspect ratios; i.e. they grow by preferentially increasing their diameter rather than their height; slow eruption rates or episodic emplacement history will build edifices with higher than average aspect ratios (e.g., Fink et al., 1993).

There are, of course, many controls other than effusion rate on the surface morphology and shapes of seamounts. They include physical parameters (e.g., eruption temperatures, lava density and viscosity), vent geometry (fissure versus point source) and underlying topography (ponding of lava in depressions, and deflection or folding of lava by substrate roughness). In addition, several volcanic edifices may be related, and connected by lateral subsurface feeder tubes (Humphris et al., 1990; Bryan et al., 1994). All of these factors must play a role (major or minor) in building the seafloor topography.

In the following we incorporate our new morphological data, and the results from the field and laboratory work described above, into existing conceptual models for magma supply at the slow-spreading MAR (e.g., Nisbet and Fowler, 1978; Sinton and Detrick, 1992; Smith and Cann, 1992, 1993). Because of the extensional environment at the ridge axis, eruptions most likely occur through fissures. We envision that small-volume eruptions through fissures commonly build small ridges; if the eruption breaks down to several points along the fissure, the ridge will be composed of a string of individual mounds. If the fissure eruption collapses to a single feeder, a hummock is formed and, when magma supply is sufficient, a hummocky seamount will be constructed. Hummocky seamounts enlarge by bulbous outgrowths and form when eruption rates are slow and steady, and cooling is rapid (enhanced in the submarine environment). A concentration of eruptions along a narrow zone within the inner valley floor leads to overlapping and piling up of the hummocky seamounts, small ridges and fields of hummocks to build an axial volcanic ridge. Occasionally, focussed eruptions with faster effusion rates and perhaps consisting of several discrete eruptive events form smooth flat top seamounts that are also associated with the axial volcanic ridge.

Hummocks cover most of the flanking deeps and gaps in the axial volcanic ridge. In some places, however, fissure eruptions with fast effusion rates form smooth-textured patches, or centralize to a single feeder to construct smooth flat top and hat seamounts. These features grow preferentially in their diameters rather than their heights. Rare voluminous eruptions with high effusion rates will spread out to cover the inner valley floor producing extensive smooth textured terrain as seen in Segment 6.

How magma is supplied to the crust to build the distinctive seafloor topography on the inner valley floor

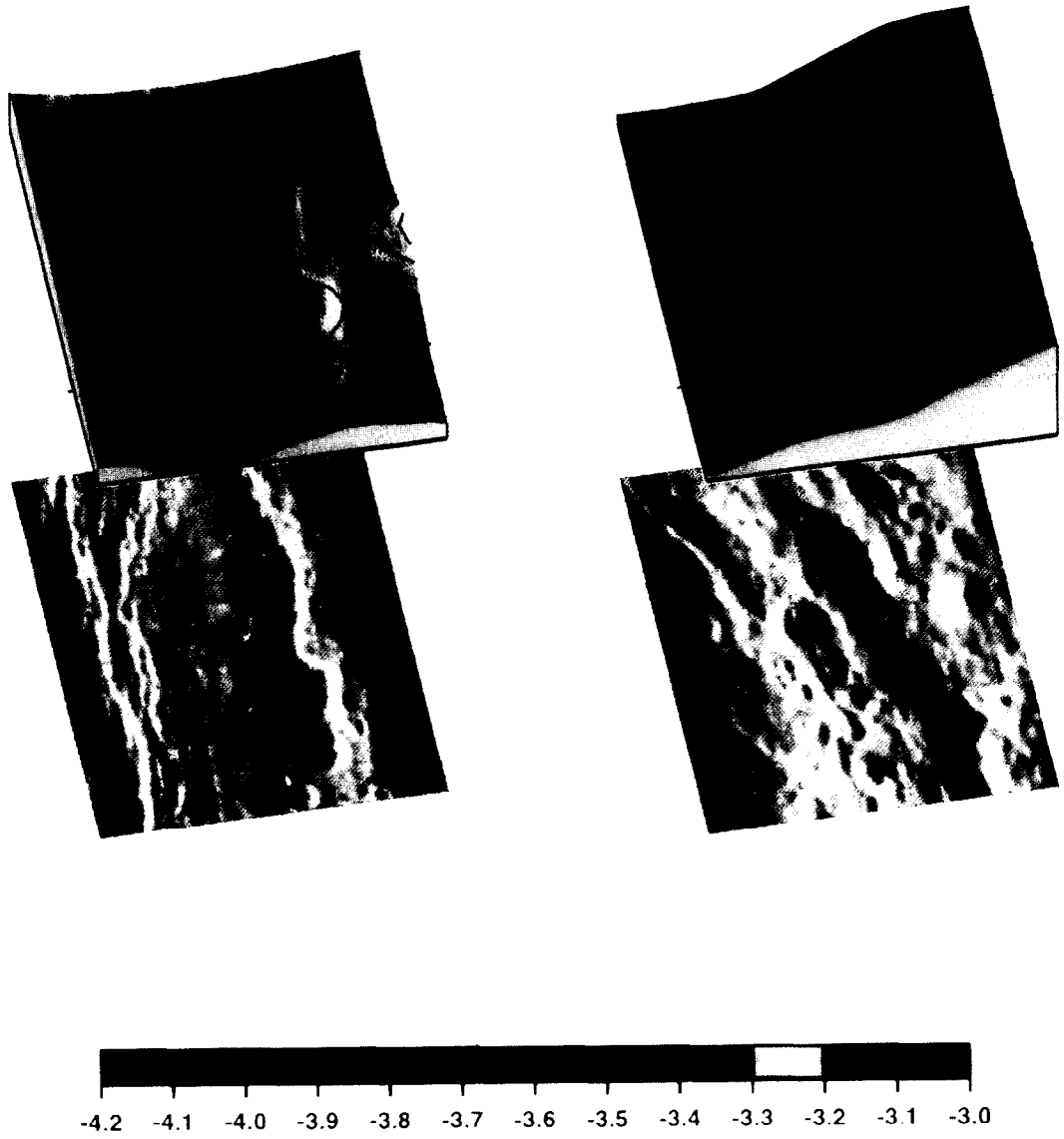

Fig. 11. Two examples of small volcanic ridges. The format of this figure is described in Fig. 7. The left panel shows "Tadpole Ridge". It is located in Segment 6 of Area 3. It is ~3300 m long, ~400 m wide, and 30 m high, on average. A circular volcano is located at the southern end. A smooth-textured brim encircles it. The along-axis orientation of the ridge mimics neighboring faults and fissures, and it is inferred to have erupted from similar fissures. The right panel shows "Caterpillar Ridge". It is located in Segment 7 of Area 4. It is at the center of the image casting a shadow to its right. It is ~2400 m high, and ~450 m wide. Its height is not well defined in the bathymetry data. Because of its segmented appearance, it is thought that an original fissure eruption collapsed to several point sources along its length.

in our study region is currently unknown. Volcanic edifices may be fed from discrete small magma bodies that rise into the crust or from small-scale instabilities that develop in an existing large crustal magma body. In the latter case, there are strong parallels to fields of monogenetic cones in continental areas on Earth (e.g.,

Heming, 1980; Hasenaka and Carmichael, 1985, 1987; Connor, 1990, Perry et al., 1990). It is, of course, impossible to constrain the crustal plumbing system from the morphology alone, which is only one piece of the puzzle. Linking these small-scale edifices with detailed rock sampling and detailed geophysical studies is the next critical step in understanding how the shallow crust is constructed at the slow-spreading MAR.

Acknowledgements

We thank the master and crew of the RV *Charles Darwin*, and the Institute of Oceanographic Sciences, Deacon Laboratory, for providing and supporting TOBI at sea. We thank Wilfred Bryan, Susan Humphris, and Kathryn Gillis for many helpful discussions. We also thank Scott C. Garland for writing the software to read and display TOBI data at sea, as well as for his help in producing the figures for this paper. Constructive reviews were provided by L. Wilson and J. Head. Funding was from the NERC and Office of Naval Research under contracts N00014-90-J-1615, and N00014-89-J-1947. W.H.O.I. contribution number 8772.

References

Abers, G.A., Parsons, B. and Weissel, J.K., 1988. Seamount abundances and distributions in the southeast Pacific. Earth Planet. Sci. Letts., 87: 137–151.

Ballard, R.D. and van Andel, Tj.H., 1977. Morphology and tectonics of the inner rift valley at lat 36°50′N on the Mid-Atlantic Ridge. Geol. Soc. Am. Bull., 88: 507–530.

Batiza, R. and Vanko, D., 1983. Volcanic development of small oceanic central volcanoes on the flanks of the East Pacific Rise inferred from narrow-beam echo-sounder surveys. Mar. Geol., 54: 53–90.

Batiza, R., Fox, P.J., Vogt, P.R., Cande, S.C., Grindlay, N.R., Melson, W.G. and O'Hearn, T., 1989. Morphology, abundance, and chemistry of near-ridge seamounts in the vicinity of the Mid-Atlantic Ridge ~ 26°S. J. Geol., 97: 209–220.

Brown, J.R. and J.A. Karson, 1988. Variations in axial processes on the Mid-Atlantic Ridge: The median valley of the MARK area. Mar. Geophys. Res., 10: 109–138.

Bryan, W.B. and Moore, J.G., 1977. Compositional variation of young basalts in the Mid-Atlantic Ridge rift valley near lat 36°49′N. Geol. Soc. Am. Bull., 88: 556–570.

Bryan, W.B., Humphris, S.E., Thompson, B. and Casey, J., 1994. Comparative volcanology of small axial eruptive centers in the MARK area. J. Geophys. Res., 99: 2973–2984.

Connor, C.B., 1990. Cinder cone clustering in the Trans Mexican Volcanic Belt: Implications for structural and petrologic models. J. Geophys. Res., 95: 19,395–19,405.

Crane, K. and Ballard, R.D., 1981. Volcanics and structure of the FAMOUS narrowgate rift: Evidence for cyclic evolution. J. Geophys. Res., 86: 5112–5124.

Detrick, R.S., Needham, H.D. and Renard, V., 1995. Gravity anomalies and crustal thickness variations along the Mid-Atlantic Ridge between 33°N and 40°N. J. Geophys. Res., 100: 3767–3788.

Epp, D. and Smoot, N.C., 1989. Distribution of seamounts in the North Atlantic. Nature, 337: 254–257.

Fink, J.H., Bridges, N.T. and Grimm, R.E., 1993. Shapes of Venusian "pancake" domes imply episodic emplacement and silicic composition. Geophys. Res. Lett., 20: 261–264. 1993.

Fowler, C.M. and Keen, C.E., 1979. Oceanic crustal structure: Mid-Atlantic Ridge at 45°N. Geophys. J. R. Astron. Soc., 56: 219–226.

Griffiths, R.W. and Fink, J.H., 1993. Effects of surface cooling on the spreading of lava flows and domes. J. Fluid Mech., 252: 667–702.

Grindlay, N.R., Fox, P.J. and Macdonald, K.C., 1991. Second order ridge axis discontinuities in the south Atlantic: Morphology, structure, and evolution. J. Geophys. Res., 13: 21–49.

Hasenaka, T. and Carmichael, I.S.E., 1985. The cinder cones of Michoacán–Guajanato, central Mexico: their age, volume and distribution, and magma discharge rate. J. Volcanol. Geotherm. Res., 25: 105–124.

Hasenaka, T. and Carmichael, I.S.E., 1987. The cinder cones of Michoacan–Guajanato, central Mexico: Petrology and chemistry. J. Petrol., 28: 241–269.

Heming, R.F., 1980. Patterns of Quaternary basaltic volcanism in northern North Island, New Zealand. N.Z. J. Geol. Geophys., 23: 335–344.

Huang, P.Y. and Solomon, S.C., 1988. Centroid depths of mid-ocean ridge earthquakes from body waveform inversion. J. Geophys. Res., 93: 13445–13477.

Humphris, S.E., Bryan, W.B., Thompson, G. and Autio, L.K., 1990. Morphology, geochemistry and evolution of Serocki Volcano. Proc. ODP Sci. Results 106/109: 67–84.

Jordan, T.H., Menard, H.W. and Smith, D.K., 1983. Density and size distribution of seamounts in the eastern Pacific inferred from wide-beam sounding data. J. Geophys. Res., 88: 10,508–10,518.

Karson, J.A. and 13 cruise participants, 1987. Along-axis variations in seafloor spreading in the MARK area. Nature, 328: 681–685.

Kong, L.S., Detrick, R.S., Fox, P.J., Mayer, L.A. and Ryan, W.B.F., 1988. The morphology and tectonics of the MARK area from Sea Beam and Sea MARC I observations (Mid-Atlantic Ridge 23°N). Mar. Geophys. Res., 10: 59–90.

Kong, L.S., Solomon, S.C. and Purdy, G.M., 1992. Microearthquake characteristics of a mid-ocean ridge along-axis high. J. Geophys. Res., 97: 1659–1685.

Kuo, B.Y. and Forsyth, D.W., 1988. Gravity anomalies of the ridge-transform system in the South Atlantic between 31 and 34.5°S: Upwelling centers and variations in crustal thickness. Mar. Geophys. Res., 10: 205–232.

Lin, J., Purdy, G.M., Schouten, H., Sempere, J.-C. and Zervas, C., 1990. Evidence from gravity data for focused magmatic accretion along the Mid-Atlantic Ridge. Nature, 344: 627–632.

Macdonald, K.C., 1977. Near-bottom magnetic anomalies, asymmetric spreading, oblique spreading, and tectonics of the Mid-Atlantic Ridge near lat 37°N. Geol. Soc. Am. Bull., 88: 541–555.

Macdonald, K.C. and Luyendyk, B.P., 1977. Deep-tow studies of the structure of the Mid-Atlantic Ridge crest near lat 37°N. Geol. Soc. Am. Bull., 88: 621–636.

Nisbet, E.G. and Fowler, C.M.R., 1978. The Mid-Atlantic Ridge at 37 and 45°N: Some geophysical and petrological constraints. Geophys. J. R. Astron. Soc., 54: 631–660.

Parson, L.M. and 16 cruise participants, 1993. En-echelon axial volcanic ridges at the Reykjanes Ridge: A life cycle of volcanism and tectonics. Earth Planet. Sci. Lett., 117: 73–87.

Perry, F.V., Baldridge, W.S., DePaolo, D.J. and Shafiqullah, M., 1990. Evolution of a magmatic system during continental extension: The Mount Taylor volcanic field, New Mexico. J. Geophys. Res., 95: 19,327–19,348.

Purdy, G.M. and Detrick, R.S., 1986. Crustal structure of the Mid-Atlantic Ridge at 23°N from seismic refraction studies. J. Geophys. Res., 91: 3739–3762.

Purdy, G.M., Sempere, J.-C., Schouten, H., Dubois, D.L. and Goldsmith, R., 1990. Bathymetry of the Mid-Atlantic Ridge, 24°–31°N: A map series. Mar. Geophys. Res., 12: 247–252.

Ramberg, I.B. and van Andel, Tj.H., 1977. Morphology and tectonic evolution of the rift valley at lat 36°30′N, Mid-Atlantic Ridge. Geol. Soc. Am. Bull., 88: 577–586.

Ramberg, I.B., Gray, D.F. and Raynolds, R.G.H., 1977. Tectonic evolution of the FAMOUS area of the Mid-Atlantic Ridge, lat 35°50′N to 36°20′N. Geol. Soc. Am. Bull., 88: 609–620.

Schmincke, H.-U. and Bednarz, U., 1990. Pillow, sheet flow and breccia flow volcanoes and volcano-tectonic hydrothermal cycles in the Extrusive Series of the northeastern Troodos ophiolite (Cyprus). In: J. Malpas et al. (Editors), Ophiolites: Ocean Crustal Analogues. Geol. Surv. Dept., Nicosia, Cyprus, pp. 185–206.

Searle, R.C. and 9 cruise participants, 1992. Volcanic and tectonic development of the Mid-Atlantic Ridge North of Kane Transform: MARNOK, 24–25°N. EOS, Abstract, 73: 569.

Sempere, J.-C., Purdy, G.M. and Schouten, H., 1990. Segmentation of the Mid-Atlantic Ridge between 24°N and 30°40′N. Nature, 344: 427–431.

Sempere, J.-C., Lin, J., Brown, H.S., Schouten, H. and Purdy, G.M., 1993. Segmentation and morphotectonic variations along a slow-spreading center: The Mid-Atlantic Ridge (24°00′N–30°40′N). Mar. Geophys. Res., 15: 153–200.

Sinton, J.M. and Detrick, R.S., 1992. Mid-ocean ridge magma chambers. J. Geophys. Res., 97: 197–216.

Smith, D.K., 1988. Shape analysis of Pacific seamounts. Earth Planet. Sci. Lett., 90: 457–466.

Smith, D.K. and Cann, J.R., 1990. Hundreds of small volcanoes on the median valley floor of the Mid-Atlantic Ridge at 24–30°N. Nature, 348: 152–155.

Smith, D.K. and Cann, J.R., 1992. The role of seamount volcanism in crustal construction along the Mid-Atlantic Ridge at 24°–30°N. J. Geophys. Res., 97: 1645–1658.

Smith, D.K. and Cann, J.R., 1993. Building the crust at the Mid-Atlantic Ridge. Nature, 365: 707–715.

Smith, D.K. and Jordan, T.H., 1988. Seamount statistics in the Pacific ocean. J. Geophys. Res., 93: 12,899–12,918.

Spencer, S. and 11 cruise participants, 1992. Nature of non-transform offsets on the Mid-Atlantic Ridge between 24 and 30°N. EOS, Abstract, 73: 553.

Toomey, D.R., Purdy, G.M. and Solomon, S.C., 1988. Microearthquakes beneath the median valley of the Mid-Atlantic ridge near 23°N: Tomography and tectonics. J. Geophys. Res., 93: 9093–9112.

Tucholke, B.E., 1991. Massive, submarine rockslide in the rift-valley wall of the Mid-Atlantic Ridge. Geology, 20: 129–132.

Whitmarsh, R.B., 1973. Median valley refraction line: Mid-Atlantic Ridge at 37°N. Nature, 246: 297–299.